広島大学 学位論文

Structural Phase Transition in $LiNbO_3$-type Ferroelectrics Studied by Synchrotron Radiation X-ray Diffraction

放射光 X 線回折による $LiNbO_3$ 型強誘電体の構造相転移の研究

2018 年

広島大学大学院理学研究科

物理科学専攻

Zhi-Gang Zhang

目　次

１．主論文

Structural Phase Transition in $LiNbO_3$-type Ferroelectrics Studied by Synchrotron Radiation X-ray Diffraction

（放射光 X 線回折による $LiNbO_3$ 型強誘電体の構造相転移の研究）

Zhi-Gang Zhang

２．公表論文

(1) Synchrotron-radiation X-ray diffraction evidence of the emergence of ferroelectricity in $LiTaO_3$ by ordering of a disordered Li ion in the polar direction.

Zhi-Gang Zhang, Tomohiro Abe, Chikako Moriyoshi, Hiroshi Tanaka, and Yoshihiro Kuroiwa,

Applied Physics Express **11,** 071501 (2018).

(2) Materials structure physics of isomorphic $LiNbO_3$ and $LiTaO_3$ ferroelectrics by synchrotron radiation X-ray diffraction.

Zhi-Gang Zhang, Tomohiro Abe, Chikako Moriyoshi, Hiroshi Tanaka, and Yoshihiro Kuroiwa,

Japanese Journal of Applied Physics, Accepted on 22 June 2018.

３．参考論文

(1) Unconventional Luminescent Centers in Metastable Phases Created by Topochemical Reduction Reactions.
Bo-Mei Liu, **Zhi-Gang Zhang**, Kai Zhang, Yoshihiro Kuroiwa, Chikako Moriyoshi, Hui-Mei Yu, Chao Li, Li-Rong Zheng, Li-Na Li, Guang Yang, Yang Zhou, Yong-Zheng Fang, Jing-Shan Hou, Yoshitaka Matsushita, and Hong-Tao Sun,
Angewandte Chemie International Edition 55, 4967 (2016).

(2) Structure fluctuation in Gd- and Mg-substituted $BaTiO_3$ with cubic structure.
Shoichi Takeda, **Zhi-Gang Zhang**, Chikako Moriyoshi, Yoshihiro Kuroiwa, Atsushi Honda, Noriyuki Inoue, Shin'ichi Higai, and Akira Ando,
Japanese Journal of Applied Physics 56, 10PB10 (2017).

主論文

Abstract

Lithium niobate ($LiNbO_3$) and the isomorphous lithium tantalite ($LiTaO_3$) undergo the phase transition from the paraelectric phase (space group: $R\bar{3}c$) to the ferroelectric phase (space group: $R3c$) with decreasing temperature. After the discovery of their ferroelectricity in 1949, these $LiNbO_3$ family crystals have attracted great attention to the applications. The Curie temperatures T_C of these two materials are fairly high as ~ 1480 and 960 K, and the spontaneous polarizations P_S at room temperature are reported to be 71 and 55 $\mu C/cm^2$, respectively. Therefore, the $LiNbO_3$ and $LiTaO_3$ crystals are expected to be a base-material for promising lead-free piezoelectric ceramics, especially for the uses at high temperatures.

Although the materials are widely used in many electronic devices, the phase transition mechanism is not clear. Some groups theoretically suggest that the phase transition is of a displacive type, which is supported by the soft modes in the phonon dispersions. However, others have not observed any soft modes near T_C, and hence argue that it should be an order-disorder type phase transition from the observed central peak mode and the results of perturbed angular correlation spectroscopy.

Regarding the order of phase transition, some groups measure the spontaneous polarization and the latent heat through T_C, and claim that the ferroelectric phase transition is of second order, which is supported by the optical properties and the dielectric susceptibilities. However, others report that the bond length changes discontinuously at T_C, which means the first-order phase transition.

The origin of the large difference in T_C and P_S between $LiNbO_3$ and $LiTaO_3$ is not clear as well. The ionic radii of the Nb and Ta ions are the same as 0.64 Å, which results in the similar crystal structure with almost the same lattice parameters *a* and *c*. The electronic structures of both materials are reported to be almost identical by the first-principles calculations, with comparable hybridization of Nb4*d*-O2*p* and Ta5*d*-O2*p* orbitals in the valence bands.

In this study, electron charge density distribution in stoichiometric $LiNbO_3$ and $LiTaO_3$ have been visualized by synchrotron radiation X-ray powder diffraction (SXRD) to adduce the conclusive evidence on the mechanism of structural phase transition and to clarify the structural origin of difference in T_C between $LiNbO_3$ and $LiTaO_3$. It is normally difficult to determine the atomic position of a light element such as Li in a material including a heavy element such as Nb or Ta by standard X-ray diffraction. The excellent counting statistics and the high angular resolution in synchrotron radiation X-ray diffraction enable us not only to determine the atomic position of the light element but also to visualize the chemical bonding nature in the electron charge density distribution maps of the materials.

The electron charge density distribution maps visualized by the maximum entropy method clearly demonstrate that the disordered Li ion along the polar direction at the two sites in the paraelectric phase is ordered at one site in the ferroelectric phase. The ordering of the disordered Li ion in the polar direction accompanied by the deformation of the oxygen octahedra gives rise to the ferroelectric phase transition. The structural change occurs continuously at the phase transition temperature, which suggests a second-order phase transition.

The clear relationships between the Nb(Ta)-O bond length, the electron charge density on the Nb(Ta)-O bond and the phase transition temperature T_C are revealed for the isomorphic structures. The Nb(Ta)-O bonding plays an important role for the elevation of T_C. The higher T_C in $LiNbO_3$ compared with the T_C in $LiTaO_3$ is attributed to the larger lattice distortion of the Nb-O oxygen octahedron in $LiNbO_3$.

The evaluated spontaneous polarization P_S by the point charge model gradually increases below T_C with decreasing temperature. The P_S evaluated from the crystal structure of $LiNbO_3$ and $LiTaO_3$ are almost the same as the results of electronic measurement, respectively, which suggests that the main contribution to the P_S of $LiNbO_3$ and $LiTaO_3$ is from the ionic polarization. The larger atomic shift of the Nb atom is considered to play an important role in the emergence of larger P_S in $LiNbO_3$.

Contents

Chapter 1

Introduction

1.1 Perovskite type dielectrics

Perovskite type oxide is a generic term for oxides having the same crystal structure as calcium titanate ($CaTiO_3$) known as the mineral name of perovskite. The general formula of the perovskite type oxide is represented by ABO_3, A and B are cations, and O is oxygen. The crystal structure with the highest symmetry is the cubic phase (space group $Pm\bar{3}m$), where the atom *A* is located at the apex of the unit lattice, the *B* atom at the body center position, and the O atom at the face center position. The structure of the cubic phase of the perovskite oxide is shown in Fig. 1-1. The *A* site is surrounded by 12 oxygen. The *B* site is surrounded by 6 oxygens and forms a BO_6 octahedron with the *B* atom on the center.

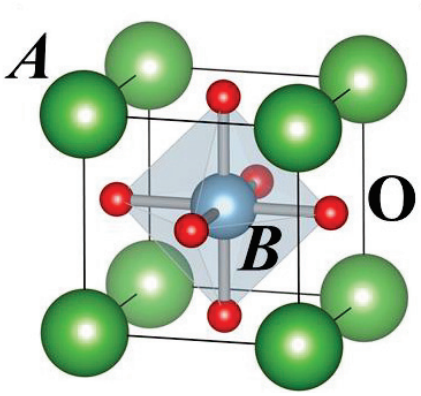

Fig. 1-1 Cubic crystal structure of perovskite type oxide ABO_3 (space group $Pm\bar{3}m$). The position of the *A* site is (0, 0, 0), the position of the *B* site is (1/2, 1/2, 1/2), and cations are arranged in each site. Oxygen is arranged at the face center positions (1/2, 1/2, 0), (1/2, 0, 1/2), (0, 1/2, 1/2) surrounding the *B* site.

Various ions make perovskite type crystals. When the valence of *A* is +2, and *B* is

+4, there are crystals such as $CaTiO_3$, barium titanate ($BaTiO_3$), lead titanate ($PbTiO_3$), and lead zirconate ($PbZrO_3$). When *A* is +1 and *B* is +5, they are potassium niobate ($KNbO_3$), lithium niobate ($LiNbO_3$) and lithium tantalite ($LiTaO_3$). When *A* and *B* are both +3, there are a few crystal such as bismuth ferrite ($BiFeO_3$) and lanthanum aluminate ($LaAlO_3$), etc.. Also, a wide variety of perovskite type solid solutions in which two or more types of perovskite type crystals are dissolved as solid are synthesized [1-3].

Table 1-1 Change in phase transition temperature and space group of representative perovskite type oxides and solid solutions [4-6]

	Curie temperature (K)	Space group		
$BaTiO_3$	403	$Pm\bar{3}m$	→	$P4mm$
	278		→	$Amm2$
	198		→	$R3m$
$BaZrO_3$	-		$Pm\bar{3}m$	
$PbTiO_3$	763	$Pm\bar{3}m$	→	$P4mm$
$LaAlO_3$	834	$Pm\bar{3}m$	→	$R\bar{3}c$
$KNbO_3$	708	$Pm\bar{3}m$	→	$P4mm$
	498		→	$Amm2$
	263		→	$R3m$
$KTaO_3$	488		$Pm\bar{3}m$	
$PbZrO_3$	505	$Pm\bar{3}m$	→	$Pbam$
$PbHfO_3$	488	$Pm\bar{3}m$	→	$R\bar{3}m$
	436		→	$Pnam$

Table 1-1 shows the valence, ionic radius, structural phase transition temperature and space group change of *A* site atoms and *B* site atoms of typical perovskite type oxides. Perovskite type crystals and perovskite type solid solution have cubic symmetry in high symmetric phases at high temperature as shown in Fig. 1-1. When the temperature decreases, the structures transfer to low symmetric phases. The crystal structure of the low symmetric phases greatly vary depending on the combination of the *A* site atoms and the *B* site atoms, and are rich in diversity. These perovskite type

crystals and their solid solution show many interesting physical properties such as dielectric properties and magnetic properties, and much research has been done from both the basic and applied aspects.

In many perovskite type oxides, structural phase transitions occur when the temperature decreases from high temperature, and the symmetry decreases. Structural phase transition is a phase transition accompanied by a slight change in crystal structure such as atomic displacement and lattice distortion among phase transitions in a crystal. Ferroelectricity and anti-ferroelectricity etc. appear when crystal phase become low symmetric phase via structural phase transition. Structural phase transitions can be caused by the spontaneous atomic displacement when the fundamental vibration of a transverse wave among the lattice vibrations which is sensitive to low temperature is frozen. As the temperature decreases from the high symmetric phase at high temperature, the frequency of this fundamental vibration decreases, that is the softening of phonon, and the soft fundamental vibration is called soft mode. The mechanism of softening is generally explained by the anharmonicity of the lattice vibrations. If the lattice vibration is anharmonic, the restoring force of lattice vibration decreases with decreasing temperature, resulting in the frequency decreasing. Upon reaching the phase transition temperature, the frequency of the soft mode becomes zero, the atomic displacement pattern corresponding to this soft mode is frozen, and a low symmetric phase is realized. Which of the lattice vibrations becomes the soft mode depends on the crystal structure, the mass of the constituent atoms, the state of thermal vibration, the bonding state and the interaction between atoms including the dipole field, etc. [7].

Two soft modes are frequently observed in perovskite type dielectrics that undergo structural transition. One is the mode at the center of the Brillouin zone, called the Γ_{15} mode, which causes a ferroelectric phase transition. The other one is the mode at the zone boundary, M_3 and R_{25} modes. Figure 1-2 shows the Brillouin zone in the cubic structure of the perovskite oxide [1]. Notation such as Γ, M, R in the phonon

mode indicate the phonon attributed to each point of Γ, M, R in the Brillouin zone.

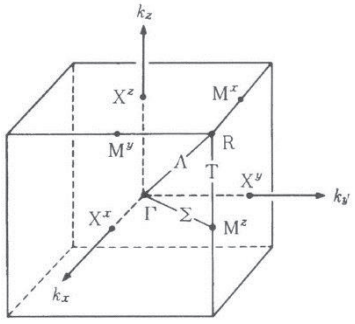

Fig. 1-2 Cubic Brillouin zone of perovskite type structure [1].

The Γ_{15} mode is a transverse wave optical (TO) mode, and when it is frozen, the atomic displacement is in the direction of [001] direction. This frozen mode causes a ferroelectric phase transition and Fig. 1-3 shows the atomic displacement in Γ_{15} mode [1], which includes the slater mode, the last mode, and the oxygen octahedral transition mode.

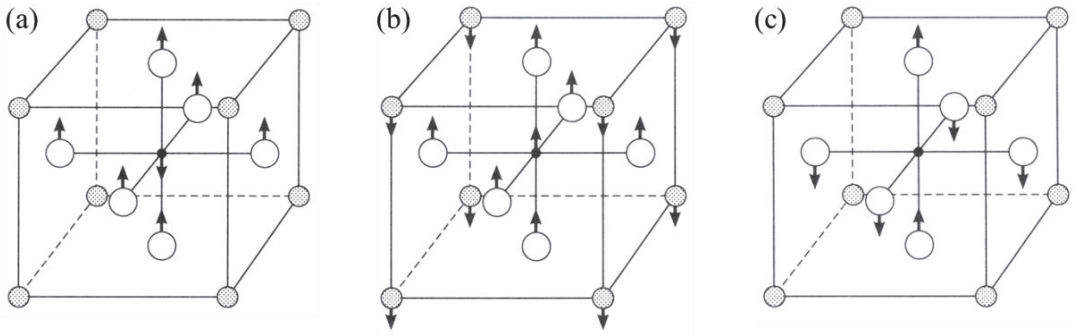

Fig. 1-3 Atomic displacement when Γ15 mode is frozen [1]; (a) slater mode, (b) last mode, (c) O octahedron displacement mode.

M_3 and R_{25} modes are transverse acoustic (TA) mode with rotational displacement of the oxygen octahedron in the crystal shown as Fig. 1-4. In the M_3 mode frozen, the upper and lower oxygen octahedrons rotate in the same direction, but in the R_{25} mode, since the rotation directions of adjacent oxygen octahedrons are different, alternate twisting of octahedrons occurs and takes a super lattice structure.

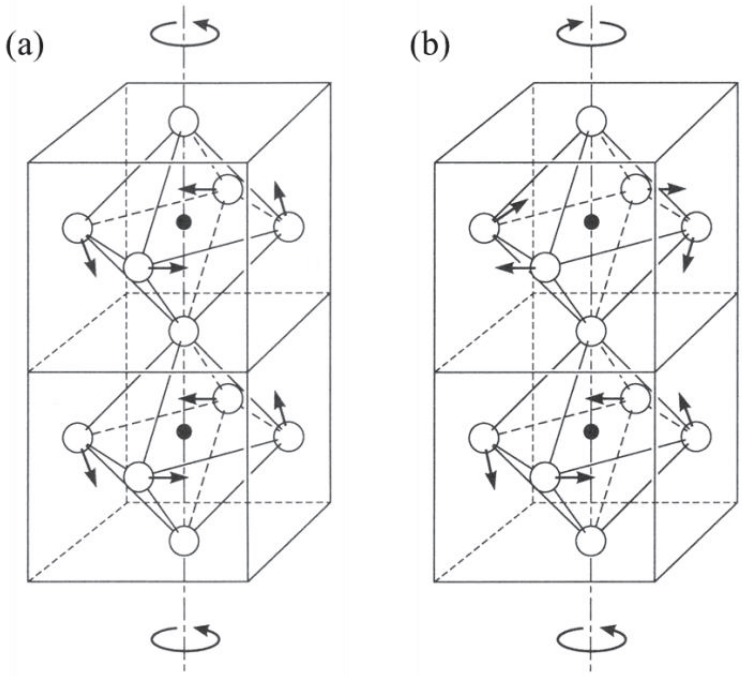

Fig. 1-4 Atomic displacement when M_3, R_{25} mode frozen [1]; (a) M_3 mode and (b) R_{25} mode.

The existence of soft modes varies widely depending on the substance. In general, in the substance in which the Γ_{15} mode is frozen, the M_3 and R_{25} modes do not freeze, and conversely the Γ_{15} mode does not occur in the substance frozen in the M_3 and R_{25} modes. This is known as separation behavior of phase transition mode in successive phase transformations [8].

On the other hand, classification by the tolerance factor t has been proposed to classify the stability of the perovskite type structure and the property of the soft mode. Tolerance factor t is a parameter representing the extent of relaxation around atoms expressed as

$$t = \frac{r_A + r_O}{\sqrt{2}(r_B + r_O)}, \tag{1-1}$$

where r_A, r_B and r_O are ionic radii of A, B and O atoms, respectively. The Shannon ion radius is often used for ionic radius [9]. The tolerance factor shows that when $t = 1$ it is an ideal perovskite structure. When $t > 1$, there is a spatial clearance around the B site rather than around the A site, and when $t < 1$, it indicates that there is clearance around the A site. Table 1-2 shows ionic radii and tolerance factors t of A site atoms

and *B* site atoms of typical perovskite type oxides. The ionic radius of the atom at *A* site with 12 coordination of the first nearest neighbor O and the ionic radius of the atom at *B* site with 6 coordination of the first nearest neighbor O are used in the calculation of the tolerance factor, respectively. In the case of the O atom, only the atom at *B* site is considered as the first nearest neighbor and the ion radius with 2 coordination is 1.35 Å.

Table 1-2 Formal number, ionic radius, tolerance factor of A site atom and B site atom of perovskite type dielectric t. The A site atom is calculated with 12 coordination, the B site atom with 6 coordination, and the O atom with 2 coordination (1.35 Å).

Materials	*A* site		*B* site		Tolerance factor *t*
	Valence	r_A (Å)	Valence	r_B (Å)	
$BaTiO_3$	2+	1.61	4+	0.605	1.071
$PbTiO_3$	2+	1.49	4+	0.605	1.027
$KNbO_3$	1+	1.64	5+	0.64	1.062
$KTaO_3$	1+	1.64	5+	0.64	1.062
$LaAlO_3$	3+	1.36	3+	0.535	1.017
$CeAlO_3$	3+	1.34	3+	0.535	1.009
$SrTiO_3$	2+	1.44	4+	0.605	1.009
$SrZrO_3$	2+	1.44	4+	0.72	0.953
$BiFeO_3$	3+	1.45	3+	0.645	0.992
$PbZrO_3$	2+	1.49	4+	0.72	0.970
$PbHfO_3$	2+	1.49	4+	0.71	0.975
$NaNbO_3$	1+	1.39	5+	0.64	0.974
$AgNbO_3$	1+	1.37	5+	0.64	0.966
$LiNbO_3$	1+	1.25	5+	0.64	0.924
$LiTaO_3$	1+	1.25	5+	0.64	0.924

In addition, Fig. 1-5 shows a correlation diagram called "Goldschmidt diagram" in which various perovskite type dielectrics are organized by ionic radii of *A* site atoms and ionic radii of *B* site atoms summarized by D. Tsuru [10]. The structure of the ABO_3 type crystal is roughly divided into two types, a perovskite type structure in

which the prototype structure is a cubic crystal structure, an ilmenite type structure and a $LiNbO_3$-type structure. In the classification of circles in Fig. 1-5, in the perovskite structure, the material in which the softening of the Γ_{15} mode occurs is red, the material in which the softening of the R_{25} mode occurs is blue, the softening of the Γ_{15} mode occurs along with the R_{25} mode frozen $SrTiO_3$ as a material is purple, structural phase transition does not occur $KTaO_3$, $BaSnO_3$, $BaZrO_3$ are shown in black, substances with ilmenite type structure and $LiNbO_3$-type structure are shown in green.

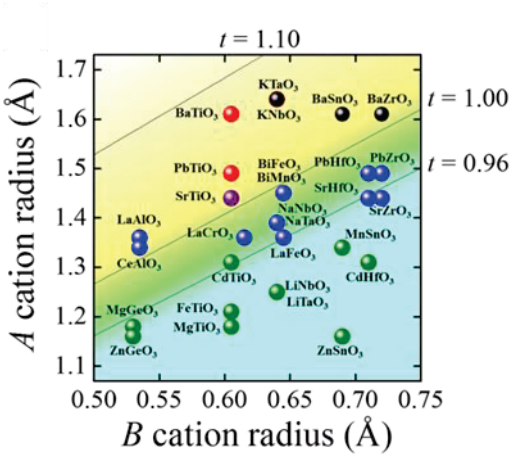

Fig. 1-5 Goldschmidt diagram. Of the perovskite type structure, the material in which the softening occurs in the Γ_{15} mode is red, the material in which the softening of the R_{25} mode occurs is blue, the material in which the softening of the Γ_{15} mode occurs, along with the freezing of the R_{25} mode, is purple, the structural phase transition is $KTaO_3$, $BaSnO_3$ and $BaZrO_3$, which do not occur, are shown in black, and substances with ilmenite type structure and $LiNbO_3$-type ilmenite type structure are shown in green.

Since the ion radius varies depending on the coordination number of the O atom, the value of the tolerance factor t slightly changes. Discussion about the tolerance factor *t* has been actively conducted [11,12]. Generally, for dielectrics with tolerance factors $t > 1$, the Γ_{15} mode, which is the zone center mode, is easily to be frozen, resulting a ferroelectric atomic displacement. On the other hand, for dielectrics with $t < 1$, the M_3 and R_{25} modes, which are on the boundary of the Brillouin zone, are easily to be frozen, resulting in anti-ferroelectric atomic displacements.

In addition, Glazer devised the symbol "Glazer notation" for classifying the characteristics of anti-ferroelectric atomic displacements such as rotation and inclination of octahedrons for substances that undergo phase transformation due to rotational displacement of oxygen octahedrons [13], where M_3 mode and R_{25} mode frozen shown in Fig.1-4 are defined as $a^0a^0c^+$ and $a^0a^0c^-$, respectively. Table 1-3 shows Glazer notation classified into 23 types [14].

Table 1-3 Classification of space groups by Glazer notation [14].

Tilt system number	Tilt system symbol	Space group	Tilt system number	Tilt system symbol	Space group
1	$a^+ b^+ c^+$	*Immm*	13	$a^- b^- b^-$	*I*2/*a*
2	$a^+ b^+ b^+$	*Immm*	14	$a^- a^- a^-$	$R\bar{3}c$
3	$a^+ a^+ a^+$	$Im\bar{3}$	15	$a^0 b^+ c^+$	*Immm*
4	$a^+ b^+ c^-$	*Pmmn*	16	$a^0 b^+ b^+$	*I*4/*mmm*
5	$a^+ a^+ c^-$	$P4_2/nmc$	17	$a^0 b^+ c^-$	*Cmcm*
6	$a^+ b^+ b^-$	*Pmmn*	18	$a^0 b^+ b^-$	*Cmcm*
7	$a^+ a^+ a^-$	$P4_2/nmc$	19	$a^0 b^+ c^-$	*I*2/*m*
8	$a^+ b^- c^-$	$P2_1/m$	20	$a^0 b^- b^-$	*Imma*
9	$a^+ a^- c^-$	$P2_1/m$	21	$a^0 a^0 c^+$	*P*4/*mbm*
10	$a^+ b^- b^-$	*Pnma*	22	$a^0 a^0 c^-$	*I*4/*mcm*
11	$a^+ a^- a^-$	*Pnma*	23	$a^0 a^0 a^0$	$Pm\bar{3}m$
12	$a^- b^- c^-$	$P\bar{1}$			

1.2 Mechanism of phase transition

At the phase transition point, the phase transition in which the crystal structure

slightly changes, such as atomic displacement or lattice distortion, is called structural phase transition. Phase transitions observed in dielectrics mostly involve structural phase transitions. Therefore, its physical properties are often discussed in the physics of the lattice system directly attributed to the crystal structure. In the structural phase transition, the fluctuation of electric polarization P, the order parameter, approaches the transition point, and the phase transition that the divergence at the transition point causes the lattice to become unstable, resulting in the ferroelectric phase transition. Some ferroelectric phase transitions are second order transitions, and others are first order transitions close to second order transitions. There are two types of ferroelectric phase transition: order-disorder type and displacive type.

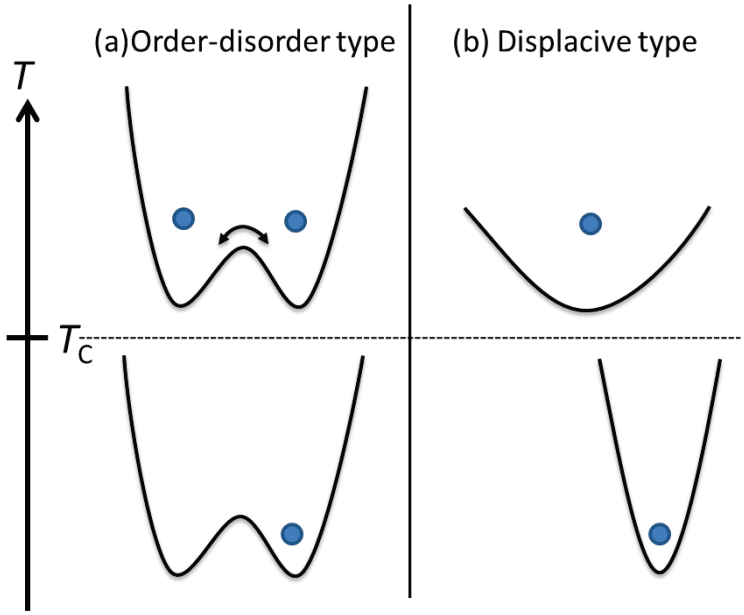

Fig. 1-6 Schematic view of atomic potential of the order-disorder and displacive type phase transitions.

Fig. 1-6 shows the schematic view of atom potentials of the two kinds of phase transition. In the order-disorder type phase transition, an atom has double potential wells and blow T_C, the atom can only occupy one of the wells. Above Tc. the atom can jump between the two potential wells. In the displacive type phase transition, the atom occupies the single potential well. With increasing temperature, near T_C, the potential becomes soft, and the atom position shifts.

In the case of the displacive phase transition, low-frequency lattice vibrations exist because long-range forces acting on ions are almost balanced with short-distance forces, and phase transition occurs due to freezing of this phonon mode. Samara et al. pointed out that short-range interactions between atoms, that is, covalent bonds are important for inducing atomic displacement of such polarity, and pointed out that the soft mode frequency ω_s that dominates the ferroelectric phase transition ω_s. It can be expressed as [15]

$$\omega_s^2 \propto [\text{Short-Range Interaction}] - [\text{Long-Range Interaction}], \qquad (1\text{-}1)$$

where Long-Range Interaction ($\sim r^{-n}$, where n is a large number ~10) is the force that an ion attempts to displace ions from the equilibrium position of the high-temperature phase by the resultant of the Coulomb force received from all the other ions, and Short-Range Interaction ($\sim r^{-n}$) is the restoring force that the ions are about to return to when they are displaced from the equilibrium position from the high-temperature phase by the lattice force that the ions receive from surrounding ions. The short-range force is closely related to the bonding state of the crystal. When the temperature is high, the short-range force is dominant, weakens as the temperature decreases, and when the short-range force becomes weaker than the long-range force, the ion loses its restoring force and the frequency of the soft mode becomes zero. The atomic displacement pattern corresponding to this soft mode is frozen and the structure of the low temperature phase is realized.

According to the mean-field approximation, a second-order displacive phase transition is associated with a soft phonon, and its frequency ω_s goes to zero as the temperature approaches a transition temperature T_C [16],

$$\omega_s^2 \propto |T_C - T|. \qquad (1\text{-}2)$$

If covalent bonding exists, Pauli repulsion is suppressed, and force is thought to act anisotropically. At this time, ω_S becomes small, and atomic displacement becomes possible at a finite temperature, so it is considered that a decrease in symmetry is

observed.

In the case of the order-disorder type, a phase transition occurs due to the interaction between invertible permanent dipoles present in the crystal. The term permanent dipole as used herein is caused by asymmetric molecular orientation or atomic displacement. Permanent dipoles in this crystal are oriented spatially disordered temporally and spatially by thermal excitation in the high temperature phase, but as the temperature decreases, the correlation between dipoles and dipoles becomes stronger and becomes aligned. Since the increase in dipole-dipole interactions slows the dipole motion, critical relaxation is observed in which the relaxation time of this dipole with respect to the external electric field increases near the phase transition temperature. At the phase transition temperature, this relaxation time finally diverges and alignment of macroscopic dipole orientation, long range order with low temperature phase symmetry appears. By further lowering the temperature, a perfect ordered state is realized. In this case, the intensity of phonon modes as well as their mode frequency remains at a finite value as $T \rightarrow T_C$, while the intensity and linewidth of a relaxation mode diverges near T_C. The temperature dependence of relaxation time τ of a relaxation mode shows a critical slowing down with a characteristic frequency τ_0 [16],

$$\tau = \frac{\tau_0 T_C}{|T - T_C|}. \tag{1-3}$$

In the displacement type ferroelectric phase transition, domains in which a certain range of unit cells are displaced in the same direction may occur as the instability due to phonon softening occurs. Therefore, it may be considered that mechanisms such as domain ordering contribute to phase transition, and in this case, disordered type appearance appears in the displacement type phase transition. In fact, some ferroelectrics show both phonon softening and critical relaxation. As described above, some ferroelectrics cannot be divided into displacement ferroelectrics and ordered disordered ferroelectrics.

1.3 Electron charge density study by SXRD

In 1912, Laue found the X-ray diffraction phenomenon by crystal for the first time in the world. In the following year, 1913, the crystal structure analysis of NaCl crystal was performed by Bragg parent and child, and the foundation of structural analysis using X-rays was established. Laue was awarded the Nobel Prize in 1914 with this accomplishment, and 100 years later, 2014 was regarded as the International Year of Crystallography decided by the United Nations. Events related to crystallography were held around the world. During the past 100 years, the crystal structure analysis by X-ray diffraction has advanced dramatically. Since diffraction is caused by X ray diffraction by interaction with electrons, the obtained diffraction peak contains information on the electron density of atoms. X-ray diffraction is an excellent technique that allows direct observation of chemical bonds in crystals in real space.

In 2001, Kuroiwa et al. first experimentally determined the electron density distribution of $BaTiO_3$ and $PbTiO_3$ by performing a powder diffraction experiment using high energy synchrotron radiation and MEM/Rietveld analysis of the obtained data [17]. Figure 1-7 and Figure 1-8 show the tetragonal phase of $BaTiO_3$ and the electron density distribution of the tetragonal phase of $PbTiO_3$, respectively. Not only the orbital hybridization between Ti-O, but also the orbital hybridization between Pb-O predicted by first-principles calculation is visualized.

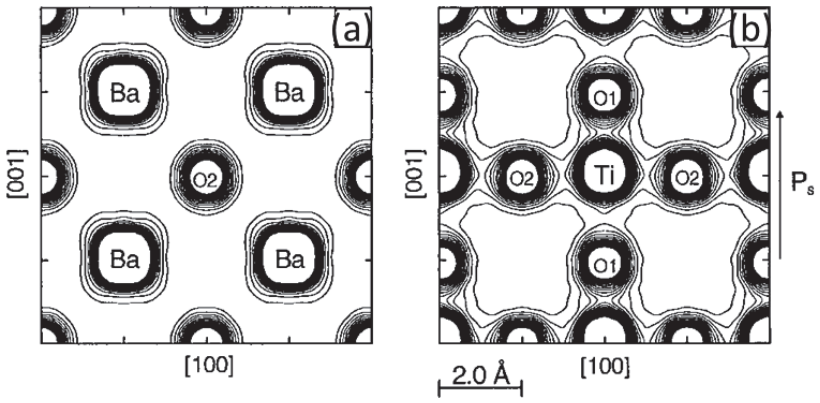

Fig. 1-7 Electron density distribution in tetragonal of $BaTiO_3$ [17]; (a) (1 0 0) plane and (b) (2 0 0) plane. Contour lines are drawn at intervals of 0.2 e/Å^3 from 0.4 e/Å^3 to 2.0 e/Å^3.

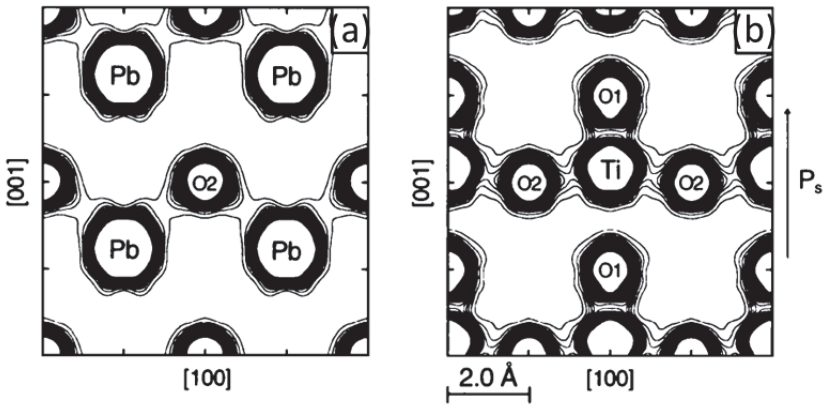

Fig. 1-8 Electron density distribution in $PbTiO_3$ tetragonal [17]; (a) (1 0 0) plane and (b) (2 0 0) plane. Contour lines are drawn at intervals of 0.2 e/Å^3 from 0.4 e/Å^3 to 2.0 e/Å^3.

In 2006, the electrostatic potential distribution and the electric field distribution of the ferroelectric phase of $PbTiO_3$ were visualized based on the Ewald's method using the same structure factor data $F(h\ k\ 1)$ [18]. Figure 1-9(a) shows the electrostatic potential, and (b) shows the electric field derived based on the electrostatic potential. The values of z component are shown colored on an equi-electron density surface of 0.86 e/Å^3, respectively. From Fig. 1-9(a), we can confirm that the Ti atom is a cation and the O atom is an anion. It is noteworthy that there is color distribution on the equi-electron density surface of Pb, that is, electronic polarization is observed.

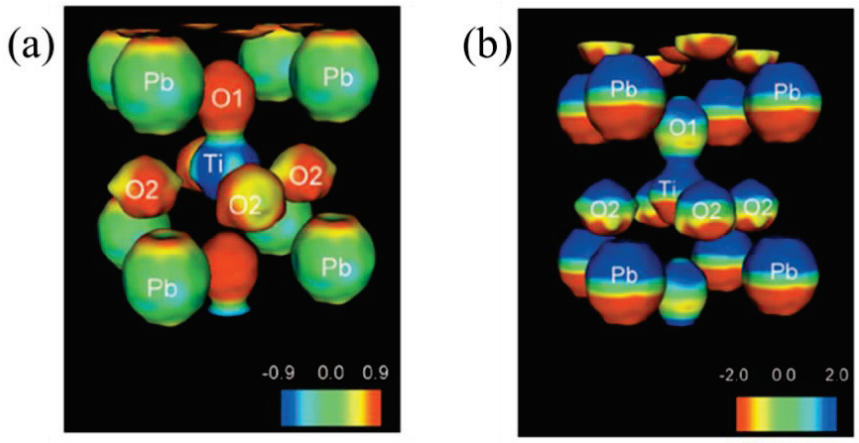

Fig. 1-9 (a) electrostatic potential distribution of $PbTiO_3$ and (b) electric field distribution of radiation powder diffraction experiment [18]. The calculation is based on the Ewald's method with the measured structural factor of $PbTiO_3$. Potential and *z* component of the electric field are colored on the equi-charge density surface 0.86 $e/Å^3$. The range is (a) -0.9 $e/Å^3$ (blue) to 0.9 $e/Å^3$ (red), and (b) -2.0 $e/Å^3$ (red) to 2.0 $e/Å^3$ (blue).

The relationship between experimentally determined electron density distribution and the rotational mode of oxygen octahedron was also studied in 2004 by Kuroiwa et al., who clarified the electron density distribution in the cubic phase of $PbHfO_3$, $PbZrO_3$, and $PbTiO_3$ with Pb at *A* site by synchrotron radiation powder diffraction experiments [19]. Figure 1-10 shows the electron density distribution in the cubic phase of $PbHfO_3$, $PbZrO_3$, and $PbTiO_3$. $PbHfO_3$ and $PbZrO_3$ in which the tolerance factor *t* is smaller than 1 exhibit an anti-ferroelectric phase transition, as compared with $PbTiO_3$ in which *t* is larger than 1 exhibits a ferroelectric phase transition. $PbHfO_3$ and $PbZrO_3$ have electron density distribution as if the oxygen octahedron would rotate. A large anisotropy on the thermal motion of the O atoms is observed. Such anisotropy is commonly observed in the perovskite type oxide which undergoes an anti-ferroelectric phase transition with the rotational mode of the oxygen octahedron.

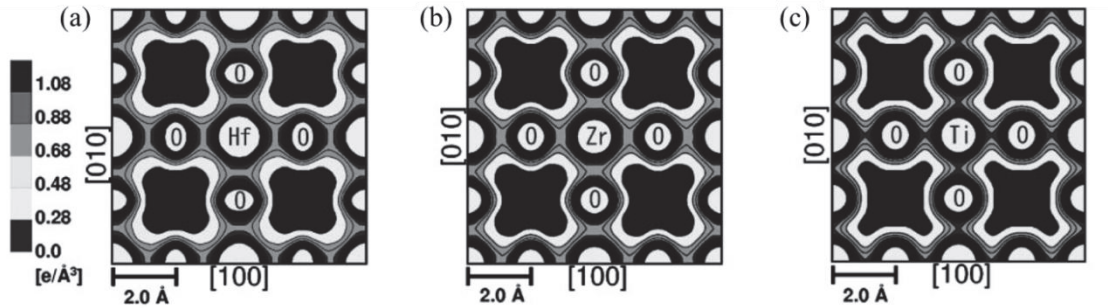

Fig. 1-10 Electron density distribution in the cubic phase of perovskite oxide with Pb at *A* site [19]. It shows the (2 0 0) plane passing through the B site and O. (a) $PbHfO_3$ at 700 K. (b) $PbZrO_3$ at 520 K. (c) $PbTiO_3$ at 800 K. Contour lines are drawn from 0.28 *e*/Å^3 to 4.28 *e*/Å^3 at intervals of 0.2 *e*/Å^3.

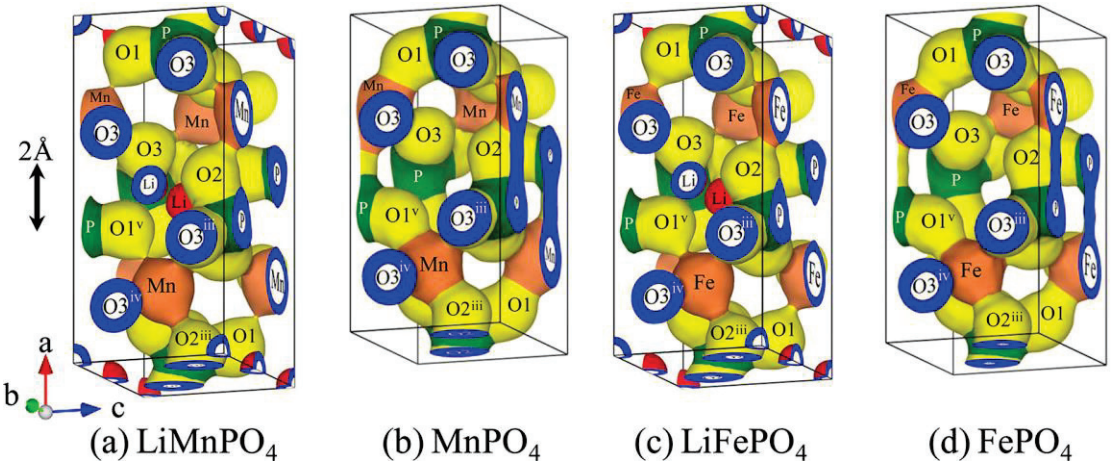

Fig. 1-11 Three dimensional (3D) charge density distributions at isosurface of 0.48 *e*/Å^3 in the unit cells for (a) $LiMnPO_4$, (b) $MnPO_4$, (c) $LiFePO_4$, and (d) $FePO_4$ [20].

On the other hand, the excellent counting statistics and the high angular resolution in SXRD also enable us to visualize the light elements such Li and Mg. Mishima et al. have already succeeded in visualizing the electron charge density distribution of the Li ions in lithium battery materials $LiMnPO_4$ and $LiFePO_4$ as contrasted with $MnPO_4$ and $FePO_4$ shown in Fig 1-11, respectively [20] . It is found that electron clouds of the Li atoms in LiMPO4 are isolated from others, which indicates the Li atom is ionic.

1.4 $LiNbO_3$ and $LiTaO_3$

Lithium niobate ($LiNbO_3$) and lithium tantalite ($LiTaO_3$) are representative material of ferroelectric optical single crystals. They were grown as a single crystal for the first time in flux method in 1949 and its ferroelectricity was reported by B. T. Matthias et al. [21]. Since then, large crystals have been grown in 1965 by the withdrawal method [22], and their properties and phase diagrams have been rapidly investigated. It can be said that it has excellent piezoelectric properties, electro-optical properties, and nonlinear optical properties and is representative oxide single crystals which have been studied numerous times in various fields [23-27]. It is particularly excellent in large crystals grown with relatively high quality and homogeneity, remarkable availability, excellent characteristics and have been applied to many optical functional elements, such as piezoelectric devices, surface acoustic wave devices, ultrasonic transducers, and optical devices [23-27]. Although some optical information devices have been put to practical use, recent developments in optical information technology have been tremendously raised, and problems related to crystals have been proposed.

The stoichiometry in the $LiNbO_3$ and $LiTaO_3$ crystals synthesized by the traditional Czochralski mothed strongly depends on the molar ratio of the Li and Nb (Ta) ions in the melt. The stoichiometric crystals can never grow from the stoichiometric melt [28-32]. Conventionally, crystals of $LiNbO_3$ and $LiTaO_3$ with a congruent composition have a Li: Nb(Ta) ratio of about 48.5: 51.5. The congruent crystals with massive vacancies normally grow to exhibit a variety of lattice parameters, spontaneous polarization P_S and phase transition temperature T_C depending on the molar ratio of Li and Nb (Ta) in the crystals [28,30,33,34]. Nowadays, using the double crucible Czochralski method [35,36] or vaportransport equilibrium (VTE) method [37], the stoichiometric crystals with higher T_C and much larger dielectric permittivity near T_C are obtained [36,38,39].

The T_C of stoichiometric $LiNbO_3$ and $LiTaO_3$ crystals are reported to be about 1480 and 960 K, respectively, which are both much higher than those of perovskite-type ferroelectrics, for example, 763 and 403 K of $PbTiO_3$ and $BaTiO_3$, respectively. The P_S of stoichiometric $LiNbO_3$ and $LiTaO_3$ crystals are 71 and 55 $\mu C/cm^2$ [38,40], respectively, which are a bit smaller than 75 $\mu C/cm^2$ of $PbTiO_3$ but much larger than 25 $\mu C/cm^2$ of $BaTiO_3$ [41]. Therefore, the $LiNbO_3$ and $LiTaO_3$ crystals are expected to be a base-material for promising lead-free piezoelectric ceramics, especially as for the high T_C, the uses at high temperatures are assumed.

Recently, $LiNbO_3$ and $LiTaO_3$ have attracted attention as its pyroelectricity, application to a very small X-ray generator and observation of cold fusion are being carried out. Pyroelectricity is a property that polarization charges appear on the surface when the crystal is heated. Utilizing its properties, a desktop X-ray generator that accelerates electrons using an electric field generated by a pyroelectric body and collides with an Au target to generate X-rays has been developed [42], and, nuclear fusion was observed at room temperature in 2005 [43]. Although this fusion is useless in the sense of power generation, it is expected to be applied as a simple neutron generator of the palm size. In this way, $LiNbO_3$ and $LiTaO_3$ have made it possible to replace the generation of neutrons and X-rays, which conventionally required large energy and large energy, with desktop equipment. Expectations are gathering for its application in the future.

1.5 Structure and phase transition of $LiNbO_3$ and $LiTaO_3$

$LiNbO_3$ and $LiTaO_3$ are known to be isomorphs, which undergo the phase transition from the paraelectric phase (space group: $R\bar{3}c$) to the ferroelectric phase (space group: $R3c$) with decreasing temperature [44,45].

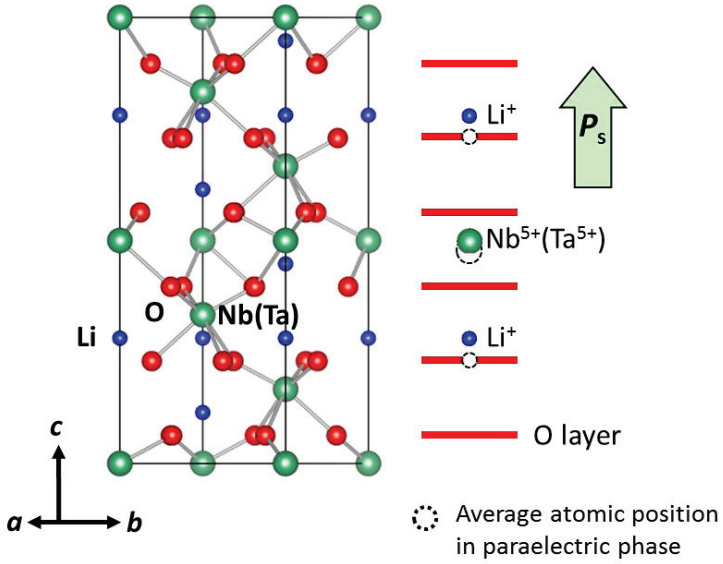

Fig.1-12 Crystal structure and spontaneous ionic displacement of $LiNbO_3$-type materials in ferroelectric phase ($R3c$)

The crystal structure of $LiNbO_3$-type materials in the ferroelectric phase are shown left in Fig.1-12. Niobium or Tantalum is surrounded by six oxygen atoms and they form an octahedron. The octahedra form a framework via the corner-shared oxygen. Lithium is located in the O-octahedron blow the Ta-O octahedron. The spontaneous ionic displacements are shown on the right side of Fig. 1-12 schematically. Oxygen atoms which have the same z-coordinate are drawn as the red line. In the paraelectric phase, the Li ion has the same z-coordinate as the Oxygen layer, and Niobium or Tantalum is located in the middle of two Oxygen layers. In the ferroelectric phase, both cations shift up along the *c*-axis and the spontaneous polarization appears upward.

Despite the wide applications in the industry, the phase transition mechanism is still chaotically discussed in the materials. In an early stage, Lines applies an effective-field theory to $LiTaO_3$, and suggests that the phase transition is of a displacive type [46], which is supported by the soft mode in the phonon dispersions [47,48]. However, other researchers have not observed any soft modes near T_C [49-51], and hence argue that it should be an order-disorder type phase transition from the

observed central peak mode [51-53] and the results of perturbed angular correlation spectroscopy [54]. Most of papers which propose the order-disorder phase transition make mention of the disorder of the Li ion in the paraelectric phase.[50,51,53,54] The theoretical studies[55,56] suggest the possibility of the disorder of O and Ta atoms, respectively, in the paraelectric phase in addition to the disorder of the Li ion.

Regarding the order of phase transition, Glass measures the spontaneous polarization and the latent heat through T_C, and claims that the ferroelectric phase transition in $LiTaO_3$ is of second order.[57] The optical properties[58,59] and the dielectric susceptibilities[60] support the second-order phase transition. However, Boysen et al. report that the Nb-O bond length in $LiNbO_3$ changes discontinuously at T_C, [61] which means the first-order phase transition. As $LiTaO_3$ and $LiNbO_3$ are analogous to one another in their basic properties, if we measure the Ta-O bond length near T_C, it may change discontinuously at T_C. Nevertheless, except the rough dilatometric measurements by Iwasaki et al. in 1967 [62], no other researchers have reported the macroscopic or microscopic changes in dimensions of the $LiNbO_3$ and $LiTaO_3$ crystal at T_C.

1.6 Purposes of the study

In general, it has been thought that it is difficult for structural analysis of materials containing light atoms by X-ray diffraction. In particular, the atomic number 3 of Li is remarkably small compared to 41 of Nb and 73 of Ta, respectively. The size of the atomic scattering factor is proportional to the atomic number, and the diffraction intensity is proportional to the square of the atom scattering factor, so the difference becomes very large, as shown in Fig 1-13. However, in order to obtain the electron density distribution and to understand the phase transition from the bonding nature between cations and the O atoms, structural analysis by X-ray is indispensable.

Although the contribution from the Li ion to the total diffraction intensity in

$LiNbO_3$ is a little larger than that in $LiTaO_3$, which means easier to determine the position of the Li ion in $LiNbO_3$. However, the Curie temperature of $LiNbO_3$ as high as ~ 1480 K and the relatively low decomposition temperature ~ 1530 K make it very difficult to measure the structural change near T_C and the charge density distribution in the ferroelectric phase. But $LiTaO_3$ has a much low T_C ~ 960 K and a much higher decomposition temperature, which is not very demanding on the heating system and give enough temperature range to allow the measurement of the detailed structural variation tendency in the paraelectric phase.

In this research, one of my aims is to investigate the crystal structure of LiNbO3-type materials by means of the high energy synchrotron radiation temperature-dependence powder diffraction experiment on $LiTaO_3$ at the electron density level and investigate the change of the structure deeply related to the phase transition mechanism.

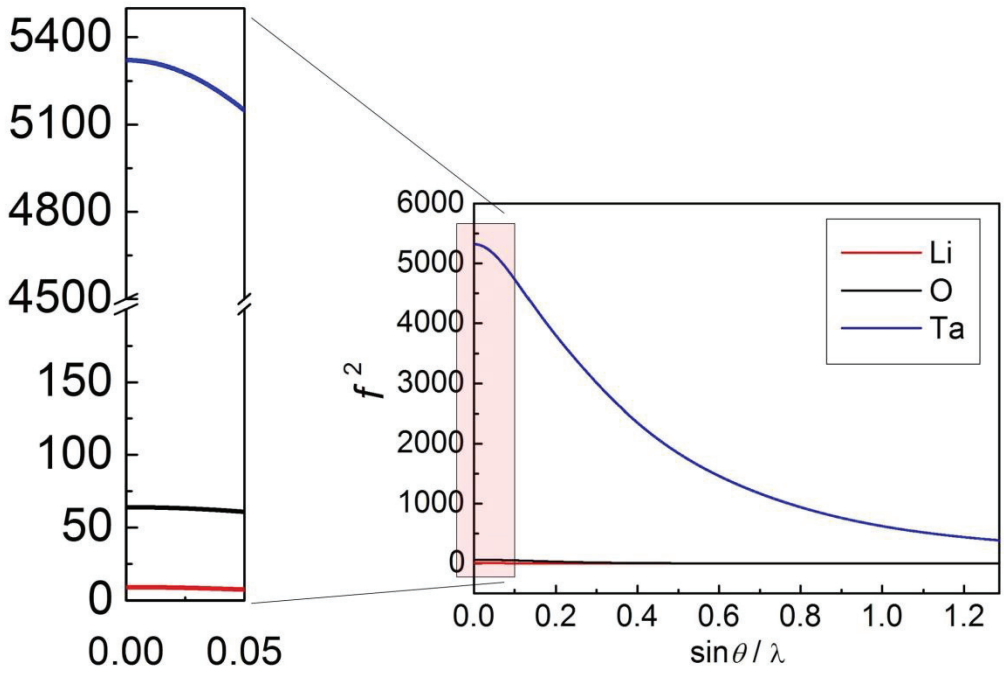

Fig.1-13 Comparison of scattering intensity of each atom obtained from atom scattering factor

On the other hand, the comparison of basic properties between $LiNbO_3$ and $LiTaO_3$ are shown in Table 1-4. The Shannon's ionic radii of the Nb and Ta ions are exactly the same as 0.64 Å for the sixfold coordination [9], which results in the similar crystal structure with almost the same lattice parameters *a* and *c* [45,61,63]. The electronic structures of both materials are reported to be almost identical by the first-principles calculations, with comparable hybridization of Nb4*d*-O2*p* and Ta5*d*-O2*p* orbitals in the valence bands [55]. However, the T_C of $LiNbO_3$ is significantly higher than that of $LiTaO_3$. In this study, we will reveal the structural characteristics which govern the T_C in the $LiNbO_3$ family crystals. The validity of estimating T_C from the crystal structures is discussed.

Table 1-4 Comparison between $LiNbO_3$ and $LiTaO_3$.

	P_S ($\mu C/cm^2$) at R.T.	T_C (K)	Electron configuration of *B*-site atom	Shannon radii (Å) of *B*-site atom
$LiNbO_3$	71	1480	[Kr] $4d^4 5s^1$	0.64 (VI)
$LiTaO_3$	55	960	[Xe]$4f^{14}$ $5d^3 6s^2$	0.64 (VI)

Chapter 2

Experiment method

2.1 Synchrotron radiation X-ray diffraction

Synchrotron radiation is the electromagnetic radiation emitted when charged particles are accelerated radially, i.e., when they are subject to an acceleration perpendicular to their velocity [64]. Today, electron storage rings are routinely employed to provide users with synchrotron radiation over a wide spectral range, from infrared to hard X-rays. Synchrotron radiation has extensive applications in determining material structures and properties in physics, chemistry, and biology, and even in disciplines such as archaeology and environmental science [65,66]. The main properties of synchrotron radiation can be summarized as: High intensity, polarization both linear and circular, broad and continuous spectral range from infrared up to the hard X-ray region, natural narrow angular collimation, pulsed time structure, high brightness of the source due to the small cross-section of the electron beam and high degree of collimation of the radiation, ultra-high vacuum environment and high beam stability, and all properties can be quantitatively evaluated.

Three generations of synchrotron-radiation sources, emitting radiation with increasing quality, have been developed to date. With the advent of third-generation synchrotron facilities shown in Fig 2-1, which are characterized by the use of insertion devices, particularly undulators, the brilliance available for researchers in the field of X-ray science has jumped by some four orders of magnitude. This enormous increase in the number of X-ray photons in tightly focused bundles has revolutionized X-ray techniques, enabling the study of increasingly small structures over shorter and shorter timescales.

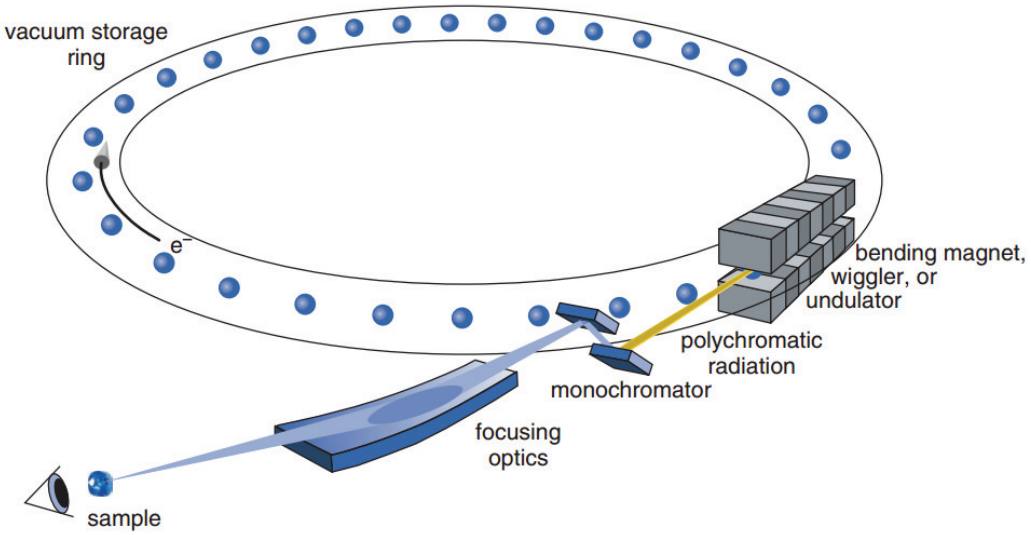

Figure 2-1 Schematic of a third-generation synchrotron [65].

In this experiment, a precise X-ray powder diffraction pattern is required, so diffraction experiments were conducted using synchrotron radiation at the large synchrotron radiation facility SPring-8 BL02B2. An advantage of radiation powder X-ray diffraction experiment is that intensity correction by extinction effect and absorption effect is not required. The extinction effect means that the diffraction intensity from the crystal deviates from the value expected from kinematic diffraction theory due to the multiple diffractions in the crystal. Also, the absorption effect means an effect of weakening the X-ray intensity by inner-shell electron excitation of an element contained in a sample. These two effects exacerbate the accuracy of the Bragg reflection intensity, especially at low angles. Information on the coupling state of electrons is contained in low-angle reflections in large amounts, and highly reliable analysis results cannot be obtained unless the reflection intensity is correctly estimated. Synchrotron radiation powder X-ray diffraction uses a powder sample with a small crystallite size as a sample and further ignores the extinction effect and absorption effect by using synchrotron radiation X rays with extremely high brightness [67].

In addition, by using synchrotron radiation with excellent angular resolution, overlapping of Bragg reflections can be alleviated. The overlap of Bragg reflections is a

disadvantage of powder X-ray diffraction, but by using synchrotron radiation it is easier to relax reflections of reflection than experimental X-ray diffraction experiments.

2.2 SPring-8 BL02B2

SPring-8 is the largest synchrotron radiation facility in the world built in Harima Science Park City, Hyogo Prefecture, Japan. The emitted radiation has a wide energy range from vacuum ultraviolet rays to hard X-rays with the world's highest luminance. Furthermore, high energy γ-ray (1.5 to 2.9 GeV) and infrared ray can also be used. Since high-energy synchrotron radiation can be used as a mobility of chemical reactions and substance changes besides structural analysis, it is used in a wide range of fields such as life science, medicine, and industry. Figure 2-2 shows a bird's eye view of SPring-8. In the generation process of synchrotron radiation, an electron beam is first generated by an electron gun ①, and the electron beam is accelerated to 1 GeV by a linear accelerator. Further accelerate to 8 GeV at the synchrotron ② and introduce it to the storage ring ③. Then, while maintaining the energy of 8 GeV, radiation light is generated by the polarization electromagnet and the insertion light source. The emitted light is guided to the hatch provided inside and outside the storage ring building through the beam line ④ and used for various experiments.

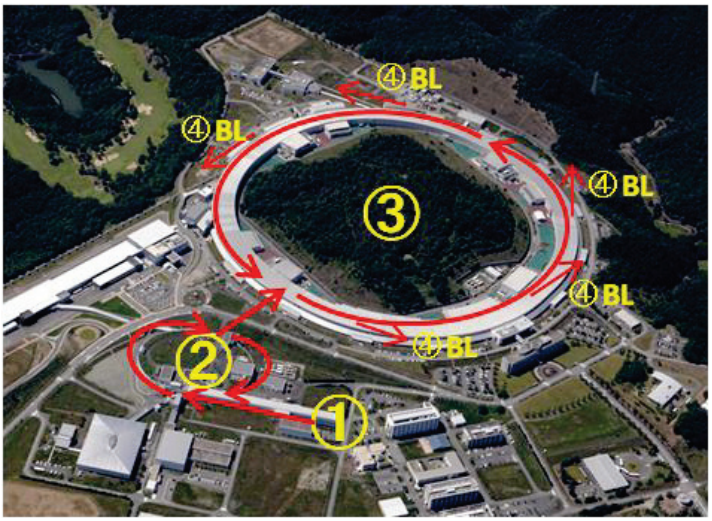

Fig. 2-2 A bird's eye view of the large synchrotron radiation facility SPring-8.

SPring-8 BL02B2 is a beam line for powder diffraction using a polarization electromagnet as a light source. Figure 2-3 shows a conceptual diagram of the optical system of BL02B2. The optical system of BL02B2 is mainly composed of a curved mirror and a dual crystal spectroscope. Mirrors are installed for the purpose of removing harmonics, etc., and they are selectively used depending on the energy of synchrotron radiation, Si for $E \leq 15.5$ keV, Ni for 15.5 keV $\leq E \leq$ 28.2 keV, and Pt for 28.3 keV $\leq$ E, respectively. The dual crystal spectrometer is installed for the purpose of improving parallelism and energy resolution, and the Si spectroscopic crystal (1 1 1) plane is used as a standard. Energy up to 38 keV can be used, and the energy resolution $\Delta E/E$ at this time is about 2×10^{-4}.

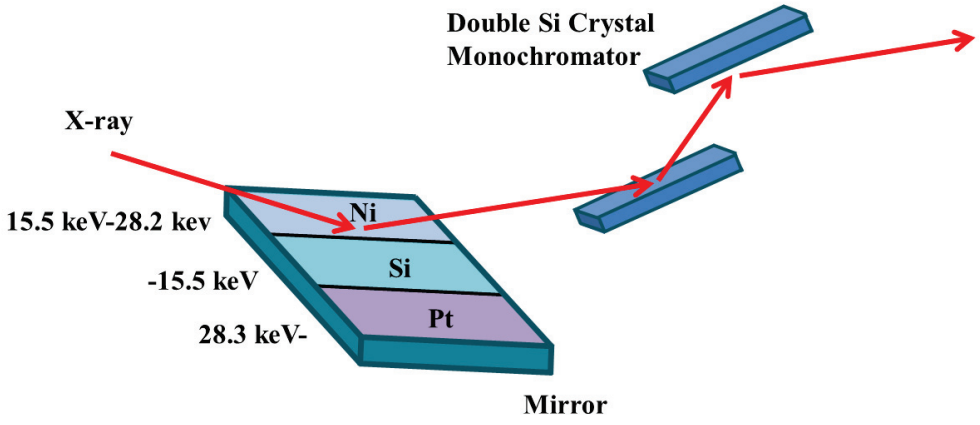

Fig. 2-3 The schematic of the optical system in SPring-8 BL02B2.

In the experiment hatch of SPring-8 BL02B2, a large Debye-Scherrer camera is installed. Figure 2-4 shows a photograph and a conceptual diagram of a large Debye-Scherrer camera. A curved imaging plate (IP) camera with a camera radius of 286.48 mm on the 2θ axis and a MYTHEN camera with a camera radius of 477.46 mm are mounted, the sample sealed in the capillary is fixed to the ω-axis and the measurement is performed by exposing the X-ray. During exposure, the sample continues to rotate around the ω-axis to minimize unevenness of diffracted X-ray intensity on Debye rings due to the particle size distribution of the sample. This is very

important in obtaining a powder diffraction pattern with high reliability. To center the sample, adjust each angle of the 5-axises gonio-head so that the sample does not move with the rotation of the ω-axis on the TV monitor which is attached to the bottom side of the camera using a CCD camera. Experiments on temperature change can be conducted with a He gas recycling type refrigerator capable of measuring at a low temperature of 15 - 300 K, a low temperature N_2 gas blowing device which can be measured at a low temperature of 90 - 300 K, a high temperature N_2 gas spraying which can be measured at a high temperature of $300^{-1}100$ K Three types of equipment are in place. In this measurement, the detector used IP and the temperature was controlled using a low temperature N 2 gas blowing device.

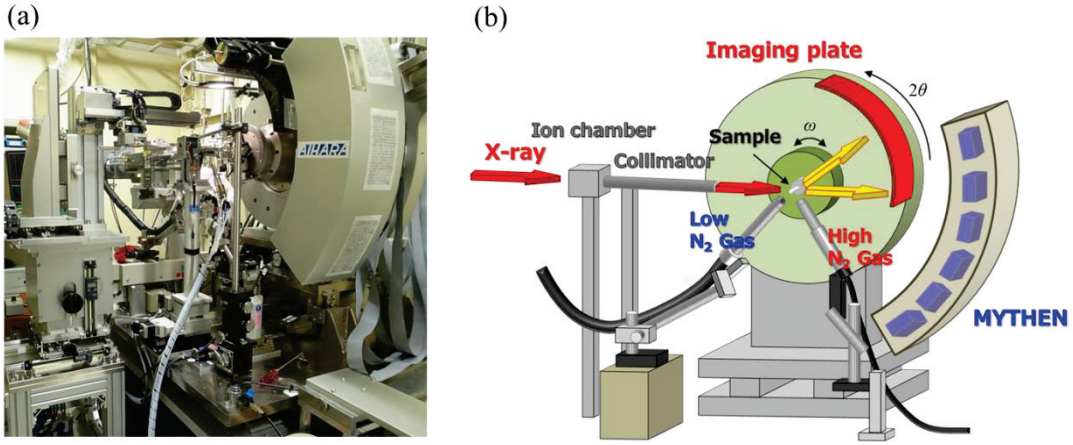

Fig. 2-4 The photograph (a) and schematic (b) of the large Debye-Scherrer camera installed in SPring-8 BL02B2 [68,69].

One of the detectors installed in the experiment hatch of SPring-8 BL02B2 is the semiconductor detector multi-connected diffractometer named MYTHEN, where six one-dimensional semiconductor detectors manufactured by DECTRIS are arranged in multiple 2θ-axes. The six detectors are aligned at intervals of one detector, and a series of data can be obtained by measuring from the reference position and from the reference position by one detector and measuring at the same time. This is the double-step mode. On the other hand, the single-step mode is used when it is desired to measure only in the vicinity of a certain angular range, and the measurement time can

be shortened by obtaining the data without displacing the detector by matching the position of the detector with the angular range. A detector with a camera radius of 477.46 mm and a size of 64 × 8 × 1 mm^3 is mounted on the 2θ-axis, the sample is fixed on the ω axis, and X-rays are exposed and measured.

The IP data is read by an offline IP reader outside the experiment hatch, but in the case of the MYTHEN camera, there is no need to read the IP and make the diffraction pattern one-dimensional, and the one-dimensional (1D) data of the diffraction pattern can be obtained rapidly in the real diffraction time. Since the diffraction angle resolution is higher than that of IP, it is possible to acquire absolute change in peak position while changing the temperature. However, since it senses even a very small intensity, the background on the low angle side becomes large. Since the IP camera detects only the intensity exceeding a certain threshold value, the background is small compared to the MYTHEN camera, and an intensity ratio with high precision can be obtained. Therefore, IP is suitable for full-pattern Rietveld refinement or electron charge density study.

2.3 Sample preparation

In conducting powder diffraction experiments, in order to obtain a highly accurate diffraction pattern, the intensity distribution of Debye rings must be uniform. If coarse crystals are mixed or the grain size is not uniform, reproducibility of the diffraction intensity decreases and Debye rings with uniform Bragg reflection intensity does not appear. In addition, when the particle diameter is 30 μm or more, the effect of the extinction effect appears, whereas when it is too small, there is a problem that the full width at half maximum of the diffraction peak widens. In order to ensure uniformity of the diffraction intensity, it is said that it is optimal to make the powder sample uniform in particle size of about 0.5 to several micrometer.

The single crystal of stoichiometric $LiNbO_3$ and $LiTaO_3$ purchased from the

Oxide Corporation were ground into powder form. In order to keep the particle size homogeneous and maintain the uniformity of the diffraction intensity, the sample powder is sorted by precipitation method, in which the sample is pulverized in an agate mortar, and the powder is stirred in ethanol and allowed to stand for 2 minutes. Since the deposition rate differs depending on the size of the particle size, powder with small particle size is dispersed above alcohol and powder with large particle size is dispersed downward. Use the difference in sedimentation rate depending on the size of this particle size, separate the ethanol containing the sample from the top to the top, the middle and the bottom, and dry them separately to make the sample uniform in particle size. Fill the capillary with the sample in the upper, middle and lower samples, and thus, a sample suitable for the measurement can be prepared.

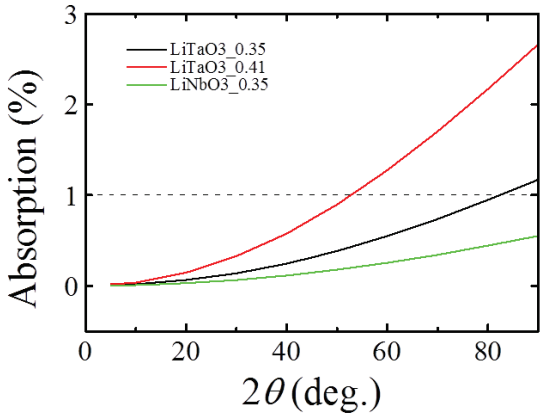

Fig. 2-4 Absorption of $LiTaO_3$ and $LiNbO_3$ within capillary 0.2 mm.

The sample powder with a homogeneous granularity was sealed into a quartz capillary. In consideration of the wavelength of the X-ray used in the experiment, the absorption coefficient of the sample, the filling rate, calculate the maximum capillary diameter which can ignore the absorption effect and use the closest capillary. The material of the capillary used is determined by the measurement temperature. Fig. 2-4 shows the absorption effect when X-ray with energy 35 keV is used and the sample packing rate is 30%. Experience has shown that the filling factor never exceeds 30%, so we calculated the absorption effect at a filling rate of 30% and used that value as a

reference. As the absorption effect is practically negligible in the range where μR is 0.3 or less and the absorption effect is 1% or less.

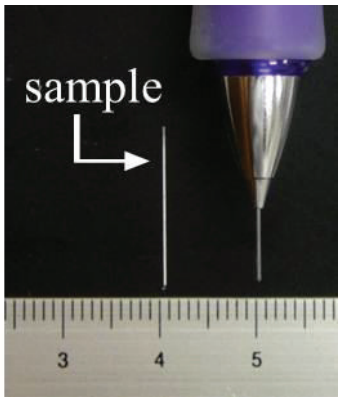

Fig. 2-5 Powder sample packed in a glass capillary with an inner diameter of 0.2 mm. The core of the mechanical pencil was placed beside for size comparison.

2.4 Experimental conditions

In this study, the powder diffraction pattern was measured using the above experimental apparatus. The point to pay attention to when deciding the energy of synchrotron radiation to use is to avoid such energy that the energy *E* of synchrotron radiation becomes slightly higher with respect to the K absorption edge energy (EK) of the constituent elements. Figure 2-6 shows the energy dependence of the absorption coefficient of atoms contained in the sample measured this time. For example, the K absorption edge of Nb is 19 keV. Therefore, when Nb is irradiated with X-rays with energies higher than 19 keV, the electrons of the K shell jump out of the bounds of the nucleus and the shell electrons in the high energy state transit to the empty inner orbital of the inner shell, The energy difference is released as characteristic X-rays. This characteristic X-ray is also called fluorescent X-ray, which causes high background intensity. Normally, in order to avoid this absorption edge and lower the background intensity, energy of 19 keV or less is used. However, in this experiment,

we considered that it is important to obtain more Bragg reflections in order to analyze the precise crystal structure of the electron density distribution level, and dare to select high energy E = 35 keV with short wavelength. As a result, the background intensity of the measurement data increases, making analysis difficult, but more diffraction data can be obtained. High energy of E = 30 keV or 35 keV was selected for all data measurement for electron density analysis.

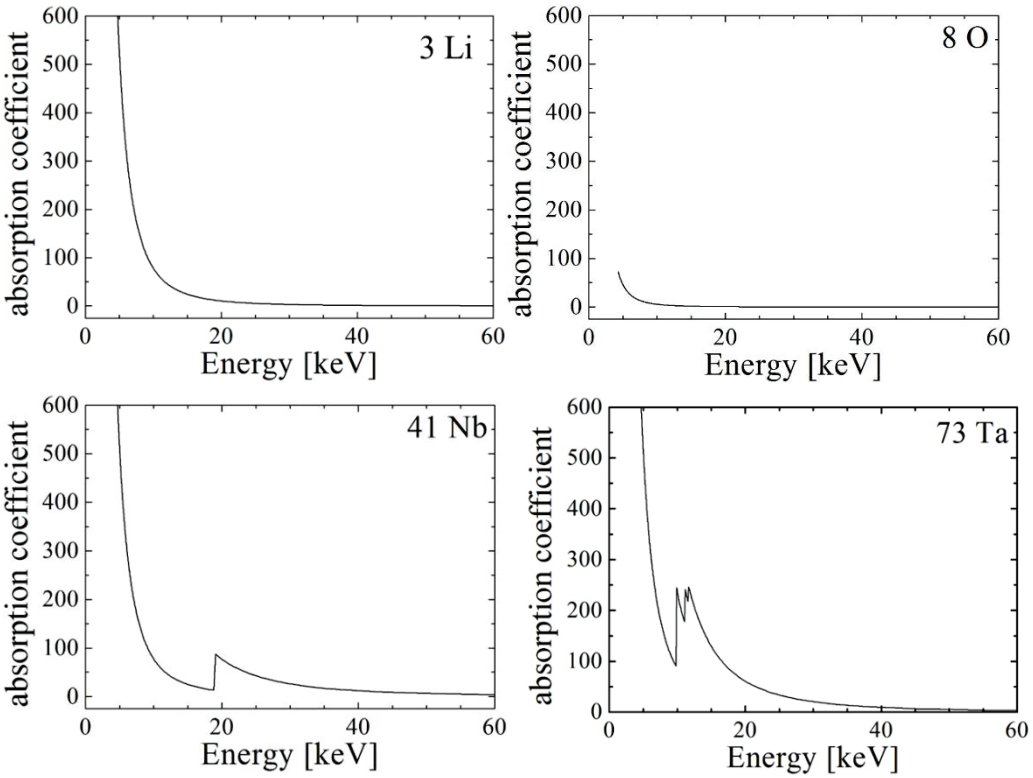

Fig. 2-6 Energy dependence of the absorption coefficient of each atom.

In order to accurately determine the electron density distribution, it is necessary to accurately determine the thermal oscillation amplitude of each atom. In order to accurately determine the thermal oscillation amplitude, it is necessary to measure high-angle data with high statistical accuracy. In general, however, it is impossible to extend the measurement time beyond the saturation time determined by the diffraction peak with low intensity of high intensity. Therefore, in this experiment, a new method was devised in order to avoid diffraction peak of low angle with high intensity and to measure the diffraction peak on the high angle side for a longer time. First, measure

the data as usual for a long time (Data low). Next, cover the lead with a lead made of lead so that low peak intensity peaks do not enter the IP, or rotate the IP camera of the diffractometer to measure the high angle diffraction peak for a long time (Data high). Two sets of data of Data low and Data high were measured in this way. The conceptual diagram of the experiment is shown in Fig. 2-7. The method of rotating the IP camera of the diffractometer has an advantage of being able to measure up to 2θ larger peak than usual. Although the method of covering the low angle side with the lead mask cannot measure up to 2θ larger than usual, there are advantages such as no error caused by rotation of the IP camera and observation of the direct beam as it is. Which 2θ can be measured depends on the sample and the temperature. In the case where a peak can be observed up to $2\theta \geq 70°$, it is measured by the method of rotating the imaging plate, and when only $2\theta < 70°$ is observed, a method using a lead mask is selected. In this sample, $LiNbO_3$ and $LiTaO_3$ were measured by a method using a lead mask. The measurement time of Data high was set to be about 4 times the measurement time of Data low.

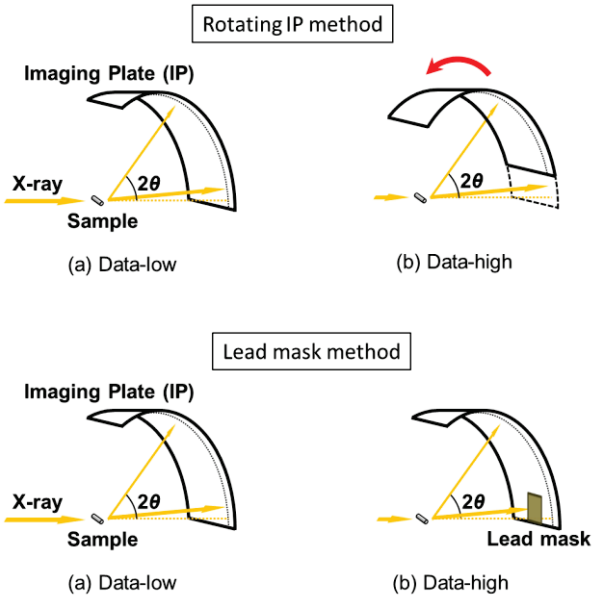

Fig. 2-7 Schematics of laboratory equipment.

High-energy X-rays with $\lambda = 0.35499(2)$ Å (Energy 35 keV) were used to detect up to the diminutive Bragg peaks with small *d*-values. In these experimental conditions,

effects of X-ray absorption for the sample could be ignored in the structure refinement. The high brilliance of synchrotron radiation X-rays enabled us to obtain high angular resolution diffraction data with good counting statistics in a short time. The diffraction pattern of $LiNbO_3$ was collected at 123 K in the ferroelectric phase to be compared directly with the structural data of $LiTaO_3$ at the same 123 K. The sample temperatures were controlled within 0.1 K using the N_2 gas flow system.

Chapter 3

Analysis method

The powder diffraction pattern obtained by synchrotron radiation X-ray powder diffraction were analyzed by the MEM/Rietveld method [70,71]. In this chapter we describe the Rietveld analysis [72], the principles and features of MEM and MEM/Rietveld analysis [73]. The programs used for the MEM/Rietveld method were provided by Prof. Makoto Sakata from Nagoya University, Prof. Eiji Nishibori from University of Tsukuba, and Prof. Masaki Takada from Tohoku University. The program package Sp6 is used for Rietveld analysis and the analysis result is shown by the program PlotPro. In addition, the program package ENIGMA [74] was used for MEM analysis. At that time, the three-dimensional electron density distribution was visualized using the program package VESTA [75].

3.1 Rietveld refinement

The Rietveld refinement has been well known as a useful method to determine the structural parameters of a crystal with given structure model based on the powder diffraction patterns since Rietveld used it to analyze the angle-resolved neutron power diffraction patterns of the atomic reactor in 1969 [72]. Nowadays, it is wildly used in the analysis of the characteristic X-ray or synchrotron radiation X-ray diffraction and time-of-fight (TOF) neutron diffraction from the spallation neutron source.

Many kinds of information can be obtained from the powder diffractions. Based on the peak position, the integral intensity of the diffraction profile and profile spreading, the lattice constants and structural parameters such as the atomic position, occupation rate, temperature factor, lattice distortion and crystallite size can be determined. Also,

the mass fraction can be obtained from the scale factors in the mixture. Rietveld analysis is a general-purpose powder diffraction data analysis technique that can simultaneously obtain these important physical quantities.

In the Rietveld analysis, the diffraction pattern calculated based on the approximate structure model is applied so that the actually measured pattern matches as closely as possible, and the information contained in the whole powder diffraction pattern is extracted to the utmost. The diffraction data measured from the powder X-ray diffraction experiment are fitted as theoretical functions through nolinear-least- squares methods.[72] The sum of the squares for the residual $S(x)$ given by

$$S(x) = \sum_i w_i [y_i - f_i(x)]^2 \tag{3-1}$$

is minimized during the optimization of the variable parameter x, where y_i (i = 1, 2, 3,…) is the observed intensity, $f_i(x) \equiv f(2\theta_i ; x_1, x_2, x\mathrm{O}_3, \ldots)$ is the theoretical intensity and w_i (=1/y_i) is the statistical weight at the ith measuring point.

Also, there is R factor as an index for evaluating the result of Rietveld analysis. There are several kinds of R factors, but R_{WP}, R_{I}, R_F are used in this research. Each definition is shown below,

$$R_{\mathrm{WP}} = \left\{ \sum_i w_i [y_i - f_i(x)]^2 \Big/ \sum_i w_i {y_i}^2 \right\}^{\frac{1}{2}}, \tag{3-2}$$

$$R_{\mathrm{I}} = \sum_H \left| I'_{\mathrm{obs}}(\boldsymbol{H}) - I_{\mathrm{cal}}(\boldsymbol{H}) \right| \Big/ \sum_H I'_{\mathrm{obs}}(\boldsymbol{H}), \tag{3-3}$$

$$R_{\mathrm{F}} = \sum_H \left\| F'_{\mathrm{obs}}(\boldsymbol{H}) \right| - \left| F_{\mathrm{cal}}(\boldsymbol{H}) \right\| \Big/ \sum_H \left| F'_{\mathrm{obs}}(\boldsymbol{H}) \right|, \tag{3-4}$$

where $I'_{\mathrm{obs}}(\boldsymbol{H})$, $I_{\mathrm{cal}}(\boldsymbol{H})$ are estimated observed values and calculated values of integrated intensity of Bragg reflection, respectively, and F'_{obs} ($\boldsymbol{H}$) is an estimated observation value of crystal structure factor. Also, $\boldsymbol{H}$ = (h, k, l). R_{WP} is a weighted reliability factor of the intensity with respect to fitting of the diffraction pattern and R_{I} and R_{F} are reliability factors comparing the calculated value and observed value for the integrated intensity and the crystal structure factor, respectively. As the reliability factor takes a smaller value, the calculated strength by the assumed structural model is

consistent, and it can be said that reliable analysis results are obtained.

When we fit each diffraction profile by Rietveld analysis, it is necessary to set the half-value width to an appropriate value, and in this research, the half-width function is defined. The half-width function defines the half width W of the profile of the calculated value estimated from the structural model. The definition formula is shown as

$$W=\left(u+v\times\tan\theta+w\times\tan^2\theta+p\times\sec^2\theta\right)^{\frac{1}{2}} \tag{3-5}$$

where u, v, w, and p are values input as parameters in Rietveld analysis, respectively. In this study, only u, v, and w are variables, and p is fixed to 0.

3.2 Rietveld analysis considering the ionic states

Crystal structure factor is defined as

$$F(\boldsymbol{k})=\sum_j f_j T_j e^{2\pi i\boldsymbol{k}\cdot\boldsymbol{r}_j}\ , \tag{3-7}$$

where the temperature factor $T(h\ k\ l)$ is expressed by a Gaussian function with $\sin\theta/\lambda$ as a variable. Since the atomic scattering factor is also an attenuation function with $\sin\theta/\lambda$ as a variable that can approximate well by Gaussian function, in order to estimate the thermal vibration parameter U_{ij} accurately, whether to make the model of atom scattering factor neutral atom or ion It is necessary to examine. Differences in values due to the model of atom scattering factors are significant in the low angle region. Figure 3-1 shows the change of atomic scattering factors of Li, Nb, Ta and O atoms with respect to the diffraction angle when X-ray with wavelength 0.35 Å (35 keV) is used. Here we are plotting all possible ion species described in International Tables for Crystallography C [76].

Since the value of f at $2\theta = 0°$ is equal to the number of electrons at that atom, f in the range $2\theta < 10°$ largely differs depending on the ion state of each atom. This influences the analysis of the temperature factor related to the attenuation factor of the

intensity. In addition, each ion in the crystal is not strictly an ionic state of a formal valence but may have a valence of a decimal value or a neutral state in some cases. Even NaCl, which is considered to be an ionic crystal, its ionicity is said to be 0.94 [77]. Therefore, if the assumption of ion valence or the analysis of temperature factor is inappropriate, the result of separated Fobs will be affected, possibly leading to erroneous electron density distribution by MEM analysis. Therefore, it is necessary to perform Rietveld analysis that is not dependent on the assumed ion state. Therefore, when aiming at precise electron density analysis, first, by fitting a temperature factor using data in a high angle range in which the values of atom scattering factors are equal regardless of neutral or ion, the thermal vibration parameter Obtained. In this study, when conducting the precise electron density analysis, data of 2θ <11.5° in $LiNbO_3$ and 2θ < 11.3° in $LiTaO_3$ are excluded, respectively. After that, Rietveld analysis was performed again using the data of the whole range without fitting the temperature factor, and Fobs for MEM analysis of the electron density was extracted.

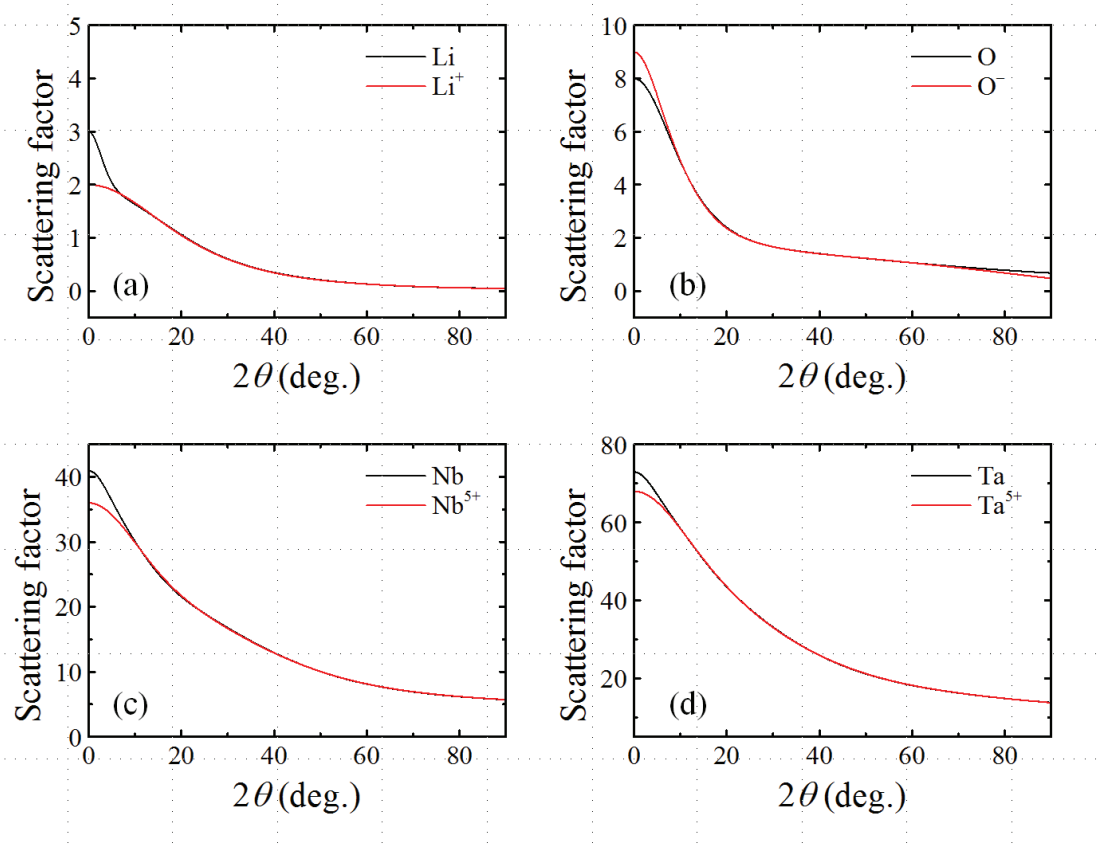

Fig. 3-1 Diffraction angle dependence of atom scattering factor *f* with x-ray of 35 keV; (a) Li,

(b) O, (c) Nb, and (d) Ta. In the low angle range, the atomic scattering factor varies depending on the ionic state. In the range of $2\theta > 20°$, the atom scattering factors of each atom are equal regardless of the ionic state.

3.3 Maximum entropy method (MEM)

The Maximum Entropy Method (MEM) is a method to derive the most probable conclusion in a controlled fashion by using information entropy (uncertainty of information to be processed) based on limited information. In 1967, it was proposed as a method of underground exploration by J. P. Burg and has made a breakthrough success in various data processes in the field of geophysics. After that, in the spotlight in the field of signal processing, its application to spectral analysis from a finite region of signal has been thriving. Today it has been applied in a wide range of fields as spectral analysis and image processing techniques.

In MEM, we obtain a solution that maximizes information entropy under the constraint that it matches the information obtained in the experiment [73]. When it is used for determination of electron / atomic nucleus density, a value that disperses the density distribution as much as possible within the range of the error with respect to the observation structural factor is estimated, and it is not zero for the truncated portion of the high angle area that cannot be measured Crystal structure factor is estimated. The main purpose of determining the electron density distribution is to observe outer shell electrons such as bound electrons and conduction electrons rather than inner shell electrons. These electrons spread spatially apart from the nucleus and are distributed and contribute greatly to the diffraction intensity of low angle reflection. When the single crystal method is used, the extinction effect becomes conspicuous in reflection in the low angle region, but correction is difficult. The MEM analysis using powder diffraction data is suitable for the visualization of chemical bonds, because the attenuation effect is negligible in the angular dispersion type powder diffraction

method and in the low angle region, the reflection hardly overlaps [71,78]. Figure 3-2 shows the structural factors obtained by MEM electron density analysis of Si and the observed structural factors [79]. The structural factor obtained by MEM electron density analysis is in good agreement with the observed structural factor, and a smooth curve is obtained also in the abortion region part in the high angle region which cannot be measured.

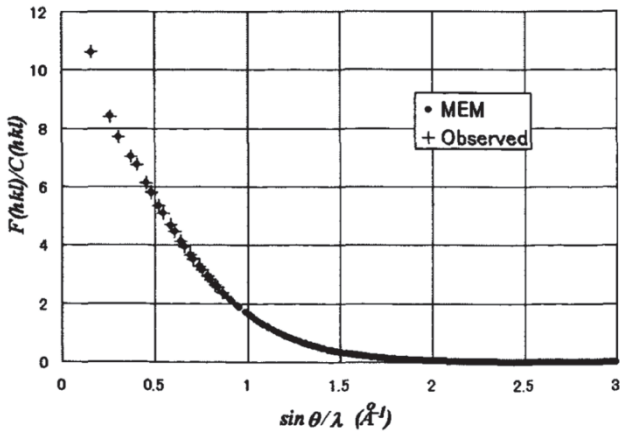

Fig. 3-2 Structural factors and observed structural factors calculated by MEM electron density analysis of Si [79]. Although the observed structural factor is only $\sin\theta/\lambda$ = 0.8 Å^{-1}, structural factors can be predicted up to the high angle region by MEM analysis.

In the case of X-rays, considering the electron density distribution in the unit lattice as one scatterer, the structural factor is defined as

$$F(H) = V\int \rho(xyz)e^{-2\pi i(hx+ky+lz)}dxdydz \tag{3-6}$$

From now on, $\boldsymbol{r} = (x, y, z)$.

Conditional entropy is

$$S = -\sum_{r} \rho'(\boldsymbol{r}) \ln \frac{\rho'(\boldsymbol{r})}{\rho'_0(\boldsymbol{r})} . \tag{3-7}$$

Here,

$$\rho'(\boldsymbol{r}) = \rho(\boldsymbol{r}) \Big/ \int \rho(\boldsymbol{r})d\boldsymbol{r} , \tag{3-8}$$

$$\rho'_0(\boldsymbol{r}) = \rho_0(\boldsymbol{r}) \Big/ \int \rho_0(\boldsymbol{r})d\boldsymbol{r} , \tag{3-9}$$

where $\rho(\boldsymbol{r})$ is the actual electron density, and $\rho_0(\boldsymbol{r})$ is the electron density in the reference state. The binding function C is

$$C = \frac{1}{N}\sum \frac{\left|F_{\mathrm{cal}}(\boldsymbol{H}) - F_{\mathrm{obs}}(\boldsymbol{H})\right|^2}{\sigma_{\boldsymbol{H}}^2}, \tag{3-10}$$

where F_{obs} $(\boldsymbol{H})$ is the crystal structure factor obtained by experiment, N is its number, and $\sigma_{\boldsymbol{H}}$ is the standard deviation for F_{obs} $(\boldsymbol{H})$. F_{cal} $(\boldsymbol{H})$ can be calculated from $\rho(\boldsymbol{r})$,

$$F_{\mathrm{cal}}(\boldsymbol{H}) = V\int \rho(\boldsymbol{r})\exp\left(-2\pi i\boldsymbol{r}\cdot\boldsymbol{H}\right)d\boldsymbol{r}. \tag{3-11}$$

C is expected to be 1 from the error theory.

From the equations (3-6) and (3-9), the following equation is obtained as the entropy $Q(\lambda)$ that has been bound,

$$Q(\lambda) = -\sum_{r}\rho'(\boldsymbol{r})\ln\frac{\rho'(\boldsymbol{r})}{\rho_0'(\boldsymbol{r})} - \frac{\lambda}{2}\left(C-1\right), \tag{3-12}$$

where λ is an undetermined multiplier of Lagrangian. Using the approximation $\partial Q(\lambda)/\partial\rho(\boldsymbol{r}) = 0$ which maximizes equation (3.10), finally,

$$\rho(\boldsymbol{r}) = \exp\left[\ln\rho_0(\boldsymbol{r}) + \lambda F_0\sum\frac{1}{\sigma_{\boldsymbol{H}}^2}\left\{F_{\mathrm{obs}}(\boldsymbol{H}) - F_{\mathrm{cal}}(\boldsymbol{H})\right\}\exp\left(-2\pi i\boldsymbol{r}\cdot\boldsymbol{H}\right)\right], \tag{3-13}$$

where $F_{\mathrm{cal}}(\boldsymbol{H})$ is approximated as a Fourier transform of $\rho_0(\boldsymbol{r})$

$$F_{\mathrm{cal}}(\boldsymbol{H}) = V\int \rho_0(\boldsymbol{r})\exp\left(-2\pi i\boldsymbol{r}\cdot\boldsymbol{H}\right)d\boldsymbol{r}. \tag{3-14}$$

The right side of the expression (3-12) is a function that depends only on $\rho_0(\boldsymbol{r})$.

When actually calculating, give a uniform electron density distribution to the first $\rho_0(\boldsymbol{r})$ and obtain the obtained $\rho(\boldsymbol{r})$ again. The operation of placing in $\rho_0(\boldsymbol{r})$ is repeated until C becomes 1 or less to obtain the electron density distribution. The electron density distribution $\rho(\boldsymbol{r})$ obtained by this method does not depend on the initial value $\rho_0(\boldsymbol{r})$, and only the accuracy of $F_{\mathrm{obs}}(\boldsymbol{H})$ is important.

Figure 3-3 shows the electron density distribution of the Si (110) plane obtained by the conventional direct Fourier method and MEM, respectively [73]. Both electron density distributions are obtained using the same actually measured structural factor $F(Q)$ included in the range of $d > 0.58$ Å ($Q < 0.86$ Å^{-1}). It is said that the electron

density obtained by the conventional direct Fourier method can be accurately derived with respect to the electron density at the atomic position. However, in order to derive the electron density distribution in the real space by the conventional direct Fourier method, it is necessary to use the structural factor of the entire inverse space (*Q*-space) in principle, so it is necessary to experimentally narrow the narrow inverse spatial range When only structural factor data is required, an unnatural distribution such as negative electron density distribution appears due to the truncation effect. In such a case, it is difficult to obtain information on distribution with low density such as bonding electrons.

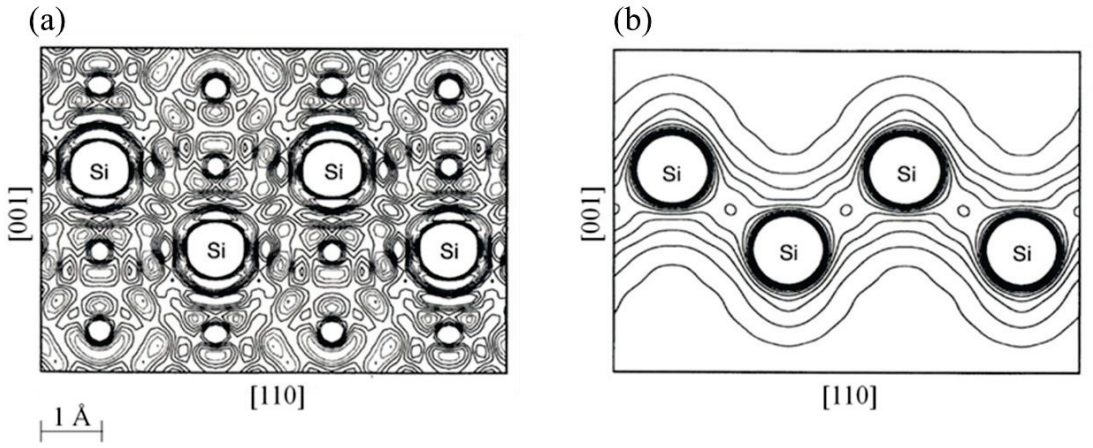

Fig. 3-3 Difference in Si electron density distribution due to different analysis method [73]; (a) the conventional direct Fourier method (contour lines -3.0 tO_3.0 eÅ^{-3}, with step 0.3 eÅ^{-3}), (b) MEM electron density analysis (contour lines 0.1 to 2.0 eÅ^{-3}, with step 0.1 eÅ^{-3}). (110) plane electron density distribution. It has been analyzed using structural factors of the same range (d > 0.58 Å) measured by X-ray diffraction experiments.

On the other hand, compared to the Fourier synthesis method, the electron density distribution obtained by MEM clearly confirms the existence of covalent bonds between Si atoms. This is to estimate the structural factor of high-Q which is not actually measured when MEM calculation is performed, and to reduce the truncation effect. Thus, in the case of the discussion of bonded electrons, MEM's method which can derive electron density distribution with less noise from finite number of structural

factors is effective.

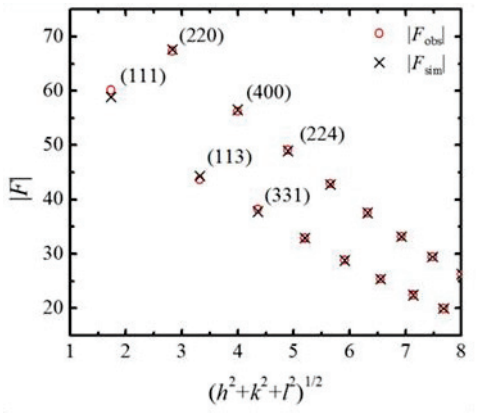

Fig. 3-4 Measured value of Si Comparison of structural factor F_{obs} and calculated value of structure factor F_{cal} by the *Pendellosung* Method [73]. Comparison between measured structure factor Fobs and F_{cal} calculated that Si is a complete ion of 4+. Fobs and F_{cal} have slight differences in low order diffraction.

In order to derive the electron density distribution, it is necessary to pay attention to what information F_{obs} (Q) predominantly includes depending on the range of Q. Figure 3-4 is a comparison between the measured structure factor Fobs used for Fig. 3-3 and the calculated structural factor F_{sim} by the *Pendellosung* Method [80], where that Si is fully ionic with +4 valence is assumed. In the range where the diffraction index is large, there is almost no difference between the measured value F_{obs} and the calculated value F_{sim}, but it is understood that the difference is large in the range where the index is small. This indicates that the information on the outer shell electrons and bound electrons is included in the small Q range of F. In order to discuss the covalent bonding nature, special attention should be paid to the estimation of F with low-Q data.

On the other hand, as already mentioned above, high-Q data is involved in aborting the Fourier transform. Q is the Bragg's equation

$$2d \sin\theta = \lambda, \tag{3-15}$$

and

$$Q = 4\pi \sin\theta / \lambda = 2\pi/d. \tag{3-16}$$

Using high-Q data we can observe a smaller d, that is to say the spatial distribution of

the electron density in the crystal in more detail. In this sense, the smallest d is used as a indication of the spatial resolution. In MEM analysis, if the F of high-Q never measured is estimated, an error may occur in the estimation. It is also effective to prevent this estimating error by using measured high-Q data. However, in the case of X-ray diffraction, since atomic scattering factors and temperature factors sharply reduce the intensity with high-Q, the statistical precision of high-Q data is generally low and conversely an incorrect analysis result might be derived. Therefore, it can be said that it is necessary to measure F_{obs} with high statistical accuracy in wide Q range from low-Q to high-Q for the analysis of MEM electron density distribution.

3.4 Weighting of MEM electron density analysis

MEM electron density analysis is a very powerful technique for visualizing the state of chemical bonding between atoms. However, in the conventional Rietveld analysis, deviations that do not take into account the intensity distribution are obtained when deriving the standard deviation of the structural factor. As a result, noise that is physically meaningless may occur in the electron density distribution by MEM. This is because MEM analysis selects "solution with the maximum information entropy" from given information. Research is being conducted to understand the trend and to visualize more accurate electron density distribution [81,82]. R. Y. De Vries et al. conducted simulations of diffraction experiments considering a virtual crystal structure with H_2O as a constituent molecule and investigated which angle range the electron density distribution derived by MEM analysis is attracted to diffraction data [83]. Figure 3-5(a) shows the crystal structure (space group $P2/m$) of H_2O considered as a model. Since the actual H_2O crystal has a three-dimensional hydrogen bond network as represented by ice I_h (space group $P6_3/mmc$), this crystal structure is a virtual crystal that they devised solely for the study of MEM. They calculated the structural factor F_{MEM} based on this structure and add Factory Error to randomly generated F_{obs}, and the error is devised to

follow the Gaussian distribution. Electron density analysis by MEM is an analysis to match the measured structural factor F_{obs} and the structural factor F_{MEM} estimated by MEM within the range of standard deviation of Fobs σ_{obs}, and unlike ordinary structural analysis, σ_{obs} is also analyzed data. Here, the standardized residual ΔF is defined as

$$\Delta F = \frac{|F_{obs}| - |F_{MEM}|}{\sigma_{obs}}. \tag{3-17}$$

If F_{MEM} is correctly estimated, ΔF only occurs due to the coincidence error of F_{obs}, so the histogram with ΔF on the horizontal axis and frequency on the vertical axis should be a Gaussian distribution.

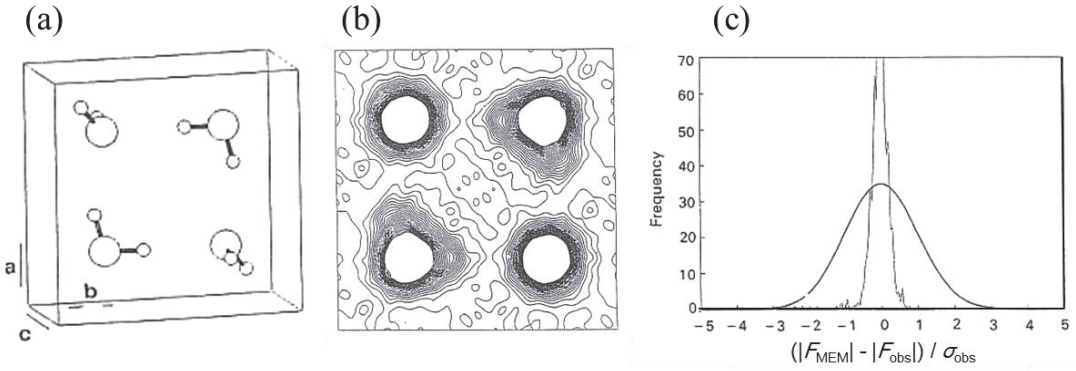

Fig. 3-5 (a) Crystal structure of H_2O, (b) MEM electron density distribution, and (c) Histogram of normalized residuals [83]. Results of MEM analysis are obtained using 1752 noisy structural factor data sets. The histogram interval of the standardized residual is 0.05. The solid line shows the ideal Gaussian distribution. The histogram has a sharp distribution, and values also exist outside the plotting range of the graph.

Figure 3-5(b) shows the MEM electron density distribution analyzed using 1752 independent structural factors F_{obs} in the range of d > 0.36 Å. Figure 3-5 (c) shows the ΔF histogram along with the ideal Gaussian distribution. There is a lot of noise in the electron density distribution, which seems to be far from the model of (a). Also, the histogram is very different from the Gaussian distribution. With a low exponent with a high intensity, data also exists in the range where $|\Delta F| > 5$. Conversely, the central part of the distribution contains many indexes with high diffraction intensity. The reason for

this distribution is based on the principle of MEM, because MEM analysis selects "solution with the maximum information entropy *S*" from given information. In the X-ray diffraction experiment, the intensity sharply decreases sharply as the higher order diffraction index, so the number of data with small diffraction intensity is generally overwhelmingly larger than the number of large data. Since the entropy *S* of MEM is larger as the diffraction intensity is smaller, excessive weights are applied to these, leading to analysis results drawn to higher order diffraction data. Conversely, with the low order diffraction data, the weight of analysis becomes excessively small, and $|\Delta F|$ becomes large. It can be seen that the electron density induced by such inappropriate weight does not reproduce the crystal structure model of the original in Fig. 3-5(a).

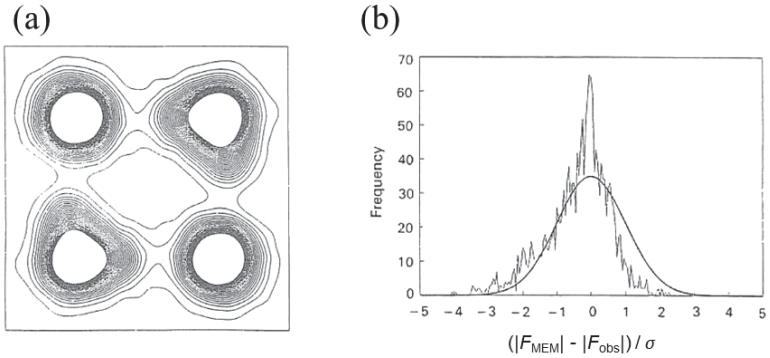

Fig. 3-6 Result of MEM analysis using weighting; (a) Electron density distribution, and (b) Histogram of normalized residuals [83]. The histogram interval of the standardized residual is 0.05. The solid line represents a Gaussian distribution graph. The histogram has an ideal Gaussian distribution shape.

R. Y. De Vries et al. proposed a weighting based on the power of reciprocal lattice vectors $|H|^{-n}$ during MEM analysis [83] as a method to alleviate such inappropriate weights. In this method, *H* is weighted and analyzed by diffraction intensity of a low order with a small value. Figure 3-6 shows the result of electron density distribution and the histogram of normalized residuals again MEM analyzed using the weight of $|H|^{-4}$. The noise of the electron density distribution is greatly reduced, and the state of hydrogen bonding is clearly visualized in addition to the strong covalent bond between

O and H. The histogram of ΔF approaches the ideal Gaussian distribution, and the components of the whole diffraction pattern fall within the range of $|\Delta F| < 5$.

As a method of mitigating the inappropriate weighting, it is effective to attach weights based on the exponentiation $|H|^{-2n}$ of the reciprocal lattice vector during MEM analysis. However, with this method, there is a tendency that the standardized residuals in the angular range where H_j is large and intensity is small are small. In order to alleviate this tendency, Yasuda et al. multiplied the bound function shown in equation (3-10) by the weight function w_j

$$C_w = \frac{1}{N_F}\sum_j^{N_F} w_j \left| \frac{F_{\mathrm{obs}}(H_j) - F_{\mathrm{MEM}}(H_j)}{\sigma_{\mathrm{obs}}(H_j)} \right|^2 \tag{3-18}$$

The weight function is based on the power $|H|^{-2n}$ of the magnitude of the reciprocal lattice vector

$$w_j = \frac{1}{|H_j|^{2n}} \left(\frac{1}{N_F} \sum_i^{N_F} \frac{1}{|H_i|^{2n}} \right). \tag{3-19}$$

Figure 3-8 shows the diffraction angle 2θ dependence of the standardized residual $(|F_{\mathrm{obs}}| - |F_{\mathrm{MEM}}|)/\sigma_{\mathrm{obs}}$ when weighting function is $n = 0$, $n = 1$. Figure 3-8 shows the histogram of $(|F_{\mathrm{obs}}| - |F_{\mathrm{MEM}}|)/\sigma_{\mathrm{obs}}$ [84]

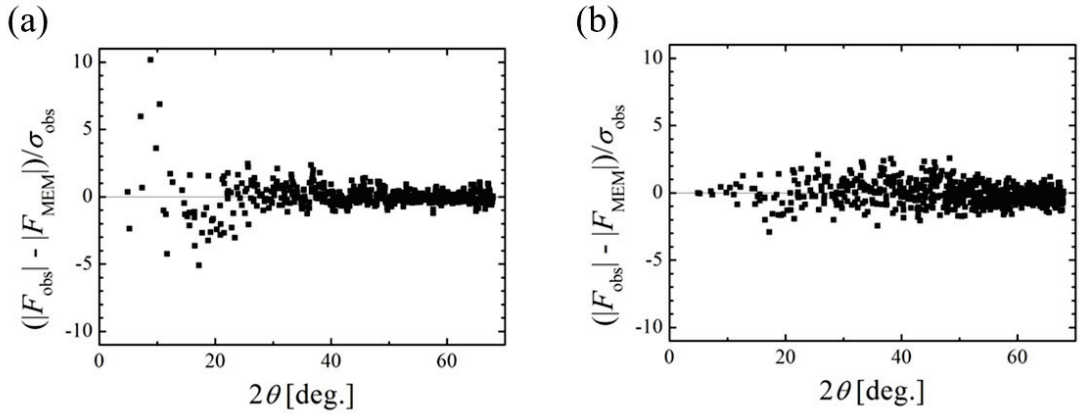

Fig. 3-7 Diffraction angle dependence of standardized residual $(|F_{\mathrm{obs}}| - |F_{\mathrm{MEM}}|)/\sigma_{\mathrm{obs}}$ in MEM electron density analysis of $PbTiO_3$ (300 K) [48]; (a) MEM Electron density analysis result without weight and (b) weighting result. If we do not weight the analysis, discrepancies in the range of $2\theta < 15°$ are conspicuous. This discrepancy is improved by weighting the analysis.

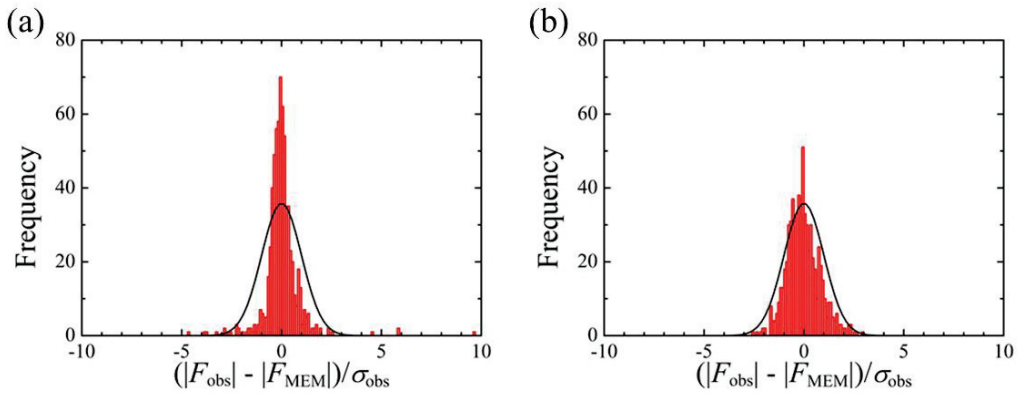

Fig. 3-8 Histogram of standardized residual $(|F_{obs}| - |F_{MEM}|)/\sigma_{obs}$ in MEM electron density analysis of $PbTiO_3$ (300 K) [48]. MEM Electron density analysis (a) Result without weight and (b) weighting result. 680 independent structural factors with d> 0.32 Å are used for analysis. The interval of the histogram is 0.1, and the solid line of black represents the Gaussian distribution of 1 in half width. By weighting, the normalized residuals are approaching the ideal Gaussian distribution.

In the case of $n = 0$, mismatches in the range of $2\theta < 15°$ are conspicuous, resulting in a sharp histogram. On the other hand, when $n = 1$, the disagreement of $2\theta < 15°$ is alleviated, the distribution becomes nearly constant irrespective of 2θ, and the histogram also has the shape of an ideal Gaussian distribution. From this, it can be seen that more accurate MEM analysis is performed by adopting weighting. Figure 3-9 shows the analysis result of 300 K electron density distribution of $PbTiO_3$ [84]. A smooth equi-charge density surface is drawn by weighting. In practice, when using this weight in this analysis, we do not change the MEM analysis program ENIGMA, which has been used conventionally, and apply a weight to the standard deviation $\sigma_{obs}(H_j)$ of $F_{obs}(H_j)$ beforehand to obtain a new $\sigma'(H_j)$, and MEM analysis was performed. The expression of $\sigma'(H_j)$ is as follows.

$$\sigma'(H_j) = w_j^{-1/2}\sigma_{obs}(H_j) = |H_j|^n \left(\frac{1}{N_F} \sum_i^{N_F} \frac{1}{|H_i|^{2n}} \right)^{-1/2} \sigma_{obs}(H_j) \qquad (3\text{-}20)$$

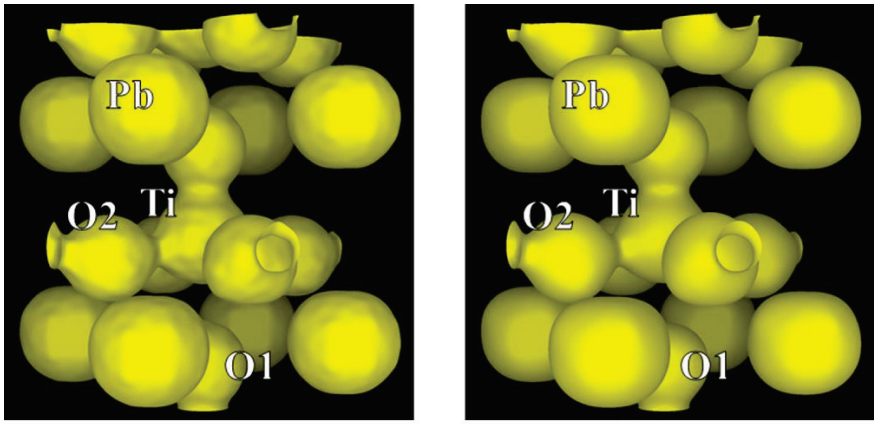

(a) (b)

Fig. 3-9 (a) Result without weight and (b) weighting result of the MEM electron density analysis result of $PbTiO_3$ (300 K). The equi-charge density surface is 0.58e Å^{-3}. When weight is not attached to analysis, irregularities are conspicuous on the surface. On the other hand, when weighting analysis, smooth distribution is obtained.

3.5 MEM/Rietveld method

Utilizing the characteristics of the Rietveld method and MEM described so far, the electron density distribution is obtained from the X-ray powder diffraction pattern by well combined MEM/Rietveld analysis. The method is described in detail as following [70,85].

In the powder diffraction experiment, all Bragg reflections are projected on the 2θ-axis, so the reflections overlap each other. Therefore, in order to obtain the electron density distribution from the powder diffraction pattern, the following process must be taken.

(1) Separating multiple overlapping Bragg reflections (profile separation) and multiplying each product of reflections

Obtain minute strength.

(2) Various corrections are applied to the obtained integrated intensity to obtain the absolute value of the crystal structure factor.

(3) Construct a crystal structure model and determine the phase of the crystal structure factor based on it.

(4) MEM analysis using the obtained crystal structure factor.

The processes (1) - (3) are performed by Rietveld analysis. In the process (1), the following profile separation is performed using the structural model that best matches the powder diffraction pattern obtained by Rietveld analysis. The measured intensity at a certain Bragg angle 2, and the calculated intensity. In this case, it is the sum ($Y_{c1} + Y_{c2} + \ldots + Y_{cM}$) of calculation intensities for M peaks. Based on this calculated intensity

$$Y_{ol}(2\theta) = Y_{o}(2\theta) \times \frac{Y_{cl}(2\theta)}{\sum_{m=1}^{M} Y_{cm}(2\theta)} \tag{3-21}$$

Yo is proportionally distributed to *M* observation intensities (Y_{o1}, Y_{o2}, …, Y_{ol}, …, Y_{oM}). Various corrections required for (2) are included in the Rietveld analysis as parameters in calculating the diffraction pattern from the crystal structure model. The process of (3) is performed using a refined crystal structure model.

Electron density distribution analysis by MEM is carried out [71] using the crystal structure factor obtained by the process of (1) to (3) of Rietveld analysis. Here, when the obtained electron density distribution conflicts with the crystal structure model, the crystal structure model is improved to coincide with the electron density distribution, and Rietveld analysis is performed again. By repeating such cycles, we finally obtain the crystal structure model and the electron density distribution which most agree with the measurement data. Figure 3-10 shows a flowchart of the MEM/Rietveld method [85].

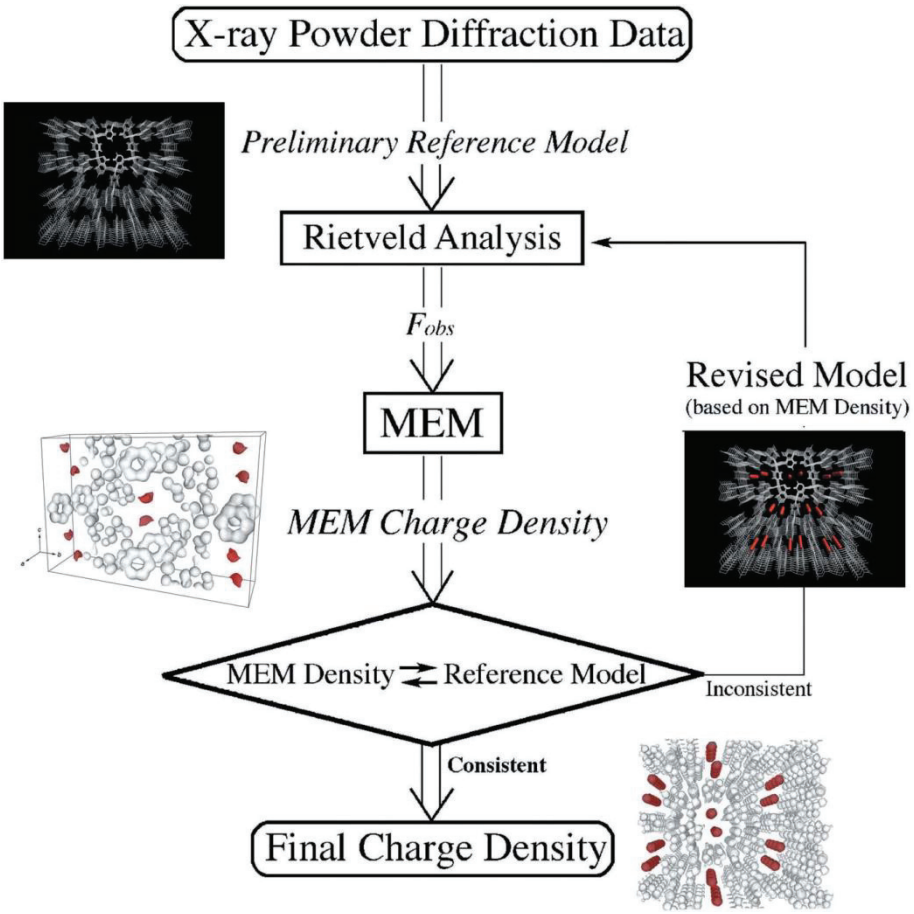

Fig. 3-10 Flow chart of the MEM/Rietveld method, modeling crystal structure and imaging charge density distribution [85].

Chapter 4

Emergence of the ferroelectric phase transition in $LiTaO_3$ by SXRD

4.1 Analysis of the structure of $LiTaO_3$ at 123 K

As mentioned before, $LiTaO_3$ contains atoms with atomic number as large as 73 for Ta and extremely small atoms with atomic number 3 for Li, so it is very difficult to determine the position of the Li ion in the crystal by X-ray. In order to analyze the structure of $LiTaO_3$ accurately, we conducted an analytical method taking advantage of the features of MEM/Rietveld method.

The MEM/Rietveld method begins by separating profiles using the Rietveld method according to the initial structural model. The structure factors are obtained by the separated profile, and utilized to calculate the electron density distribution by MEM analysis. However, if there are errors in the structural model, there will be portions that cannot be separated in profile separation. The structural factor coming from that part affects the electron density distribution obtained by MEM analysis, and if there is a difference between the electron density distribution and the structural model, the ghost peak indicating that there is an error in the structural model within the electron density distribution. Nevertheless, in reverse, this feature is being used in the analysis.

Fig. 4-1 Debye Scherrer patterns recorded on the imaging plate (IP).

The Debye Scherrer patterns of the low-angle and high-angle data of $LiTaO_3$ (123 K, rhombohedral phase with space group *R*3*c*) obtained by synchrotron radiation powder diffraction experiment is shown in Fig. 4-1. In this photograph, the darker black color means that the diffraction intensity is larger. The picture of the high-angle data appears wholly darker than the low-angle data because the measurement time is long and the absolute value of the background is large. MEM/Rietveld analysis was performed with the one-dimensional data made by integrating the intensity of this diffraction image with a width of 2.5 mm (51 pixels) corresponding to the diffraction angle 2θ.

Initially we analyzed the diffraction patterns using a structural model assuming the TaO_3 structure shown as Fig. 3-2(a), which consists of only one Ta atom and three O atoms, which does not contain Li. MEM/ Rietveld analysis is performed and the electron density distribution obtained is shown in Fig. 4-2(b). It can be seen that there is an electron cloud which does not exist in the structural model at the part surrounded by the red circle. This electron cloud is considered to be an electronic cloud of Li.

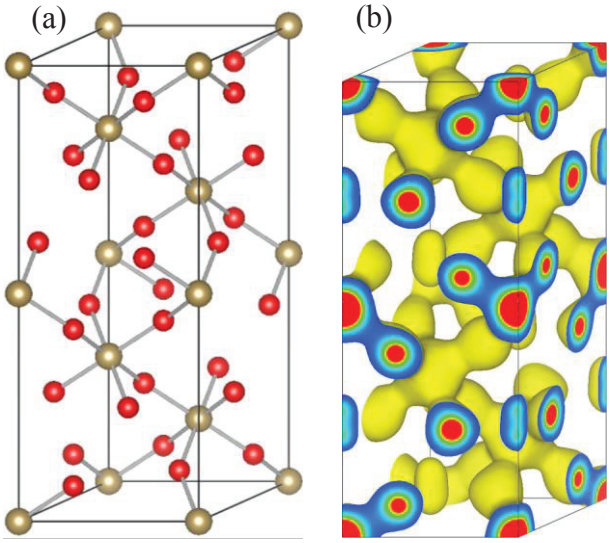

Fig. 4-2 (a) Structure model without Li in low temperature phase and (b) results of analysis using a structural model without Li. (0.5 e/Å^3)

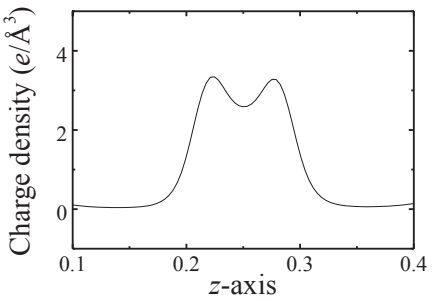

Fig. 4-3 One-dimensional charge density distribution along c-axis near $z = 0.25$.

When we plotted the one-dimensional (1D) charge density distribution along *c*-axis in Fig. 4-3, it was found that he electron cloud extends in the c-axis direction, and this electron cloud is made by two sites at $z \approx 0.223$ and 0.277. It is naturally thought that the Li ion is located at the two sites. In the hexagonal unit cell of space group *R*3*c*, the Ta atom occupies the 6*a* site, which is on the c-axis and the O atom occupies the 18*b* site, which is out of the c-axis. According to the charge density distribution for the Li atom, the two possible sites are both the 6*a* site. To make the number of the Li atom the same with the Ta atom, the total occupancy of Li at the two site should be 1, which means there are vacancies at a half part of the positons of the Li ions. In the 1D charge density distribution, the peaks of the two Li site has similar values, which means the Li ions occupies the two site with equal possibility. However, it is not very exact. To obtain the occupancy of the Li ion, the refinement of Li occupancy is necessary.

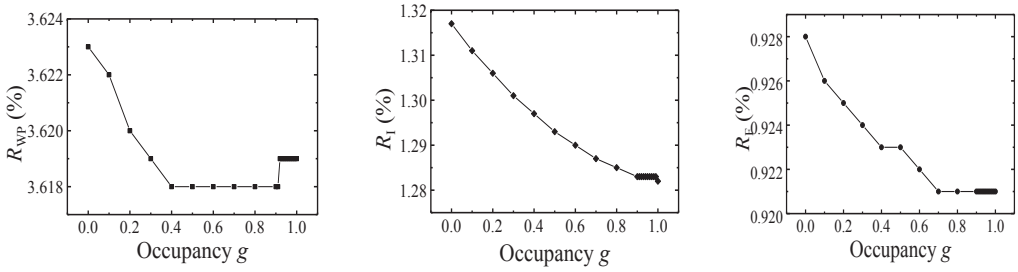

Fig. 4-4 *R* factors as functions of the occupancy of Li on the up site.

In the refinement of Li occupancy, the occupation rate of Li was obtained by manually changing the occupation rate comparing the value of the reliability factor *R* factors of each occupation rate. Regarding the occupation ratio, the occupation ratio of Li with the lager *z*-coordinate is defined as *g*, and the occupation rate of Li as the smaller coordinate is taken as $(1 - g)$. Then, the value of the reliability factor R_{WP}, R_I and R_F as functions of the occupancy of the Li ion at the up site changing from 0 to 1 with the step 0.1 are shown in Fig. 4-4. It can be found that the R_I is much more sensitive to the occupancy of the Li ion than R_{WP} and R_F. So, R_I was chosen as the

indicator to determining the occupancy of the Li ion. R_I charges smaller with the increasing of occupancy in the whole range and becomes the smallest at g = 1. The reliability factor is the best at g = 1, and Li is considered to occupy one site. Note that the step of occupancy has been set to 0.01 near g = 1. So it is very reliable that the Li ion is fully ordered at the up site near z = 0.277, which is normal at the very low temperature.

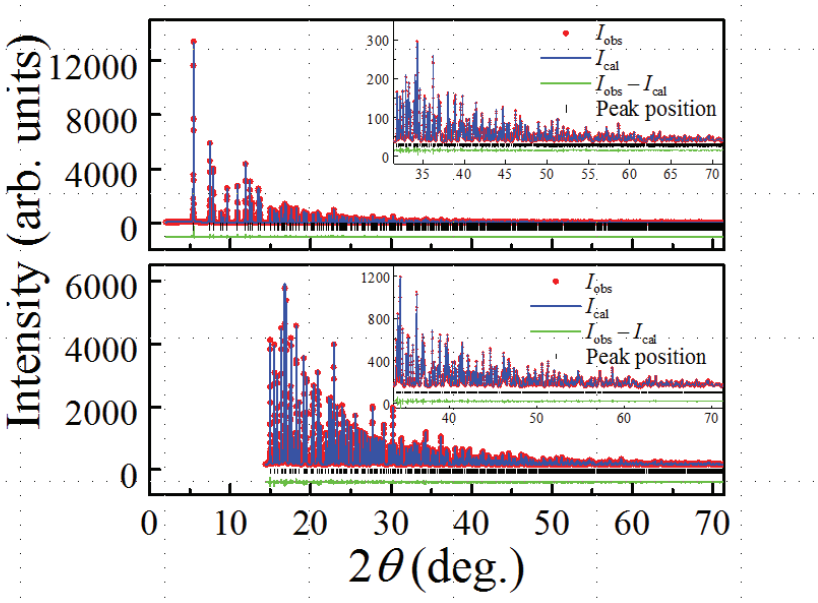

Fig. 4-5 Fitting diffraction patterns of $LiTaO_3$ at 123 K.

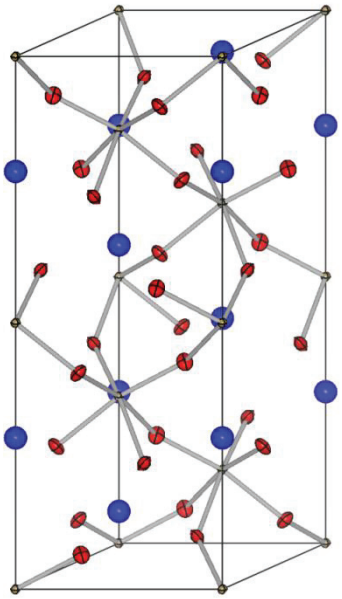

Fig. 4-6 Structure of $LiTaO_3$ at 123 K with the thermal ellipsoids 99% probability.

With the determined site and occupancy for the Li ion, the Rietveld refinement with all the parameter fitted was performed. The analysis range is $2\theta < 71.4°$ ($d > 0.304$ Å). In the final structural model, we applied ionic models for atomic scattering factors, an anisotropic model for thermal vibration parameters of the Ta atom and O atoms, and an isotropic model for thermal oscillation parameters of the Li atom. The position of the Li ion is refined very careful, and finally, the position of the Li ion is converged at z = 0.2841(4), which is very close to the position z= 0.277 indicated by the charge density distribution of assumed structure TaO_3 initially. The confidence factor is sufficiently small with R_{WP} = 2.89%, R_I = 1.23%, and R_F = 0.84%, which shows that fitting is done well. The structure of $LiTaO_3$ at 123 K is shown as Fig. 3-6 and detailed structure parameters are listed in the Table 3-1.

Table 3-1 Ferroelectric phase at 123 K. Space group: $R3c$. Lattice parameters: a = 5.14359(1) Å and c = 13.78143(2) Å. R_{WP} = 2.89%, R_I = 1.23%, and R_F = 0.84% for data with $d > 0.304$ Å.

Atom	*x*	*y*	*z*	*occupancy*	U_{11} or U_{iso}	U_{22}	U_{33}	U_{12}	U_{23}	U_{13}
Li	0	0	0.2841(4)	1	0.205(1)	-	-	-	-	-
Ta	0	0	0	1	0.117(2)	= U_{11}	0.100(5)	0.058(1)	0	0
O	0.3832(3)	0.3736(3)	0.2355(1)	1	0.296(40)	0.29(17)	0.35(13)	0.12(9)	-0.048(93)	-0.14(10)

4.2 Analysis of the structure of $LiTaO_3$ at 123 K and Bond Valence Sum (BVS) study

The Debye Scherrer patterns of the low-angle and high-angle data of $LiTaO_3$ (1050 K, rhombohedral phase with space group $R\bar{3}c$) obtained by synchrotron radiation powder diffraction experiment is shown in Fig. 4-7. We used the same method introduced in last part by assuming the TaO_3 structure to get some clues of the Li ion site. Similarly, two maximum points of the charge density distribution were found. As

the centrosymmetric property of the space group $R\bar{3}c$, if we assume that the positions of the maxima of the charge density distribution are the position of the Li ions, the Li ions must be located at the two positions will equal probability, which is different with the structure at 123 K without centrosymmetric space group.

Fig. 4-7 Debye Scherrer patterns of $LiTaO_3$ in the paraelectric phase at 1050 K recorded on the imaging plate.

With the determined site and occupancy for the Li ion, the Rietveld refinement with all the parameter fitted was performed. The analysis range is $2\theta < 57.0°$ ($d > 0.458$ Å). In the final structural model, we applied ionic models for atomic scattering factors, an anisotropic model for thermal vibration parameters of the Ta atom and O atoms, and an isotropic model for thermal oscillation parameters of the Li atom. Finally, the positions of the Li ion is converged at $z = 0.278(1)$ and the centrosymmetric position $z = 0.222(1)$. The confidence factor is sufficiently small with $R_{WP} = 4.85\%$, $R_I = 1.33\%$, and $R_F = 1.35\%$, and the fitting diffraction pattern is shown as Fig. 4-8. The structure of $LiTaO_3$ at 1050 K is shown as Fig. 4-9(a) and detailed structure parameters are listed in the Table 4-2(a). We have confirmed the validity of the Li ion fully ordered at $z = 0.25$ in the paraelectric phase. The reliability factor became worse as $R_{WP} = 5.036\%$, $R_I = 2.355\%$, and $R_F = 1.846\%$, and the displacement parameter of the Li ion showed an unusually large values as $U_{iso} = 0.48$ Å^2.

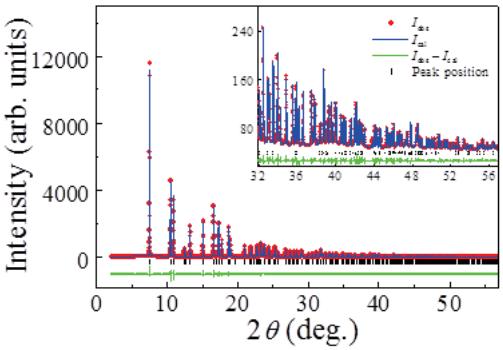

Fig. 4-8 Fitting diffraction pattern of $LiTaO_3$ at 1050 K.

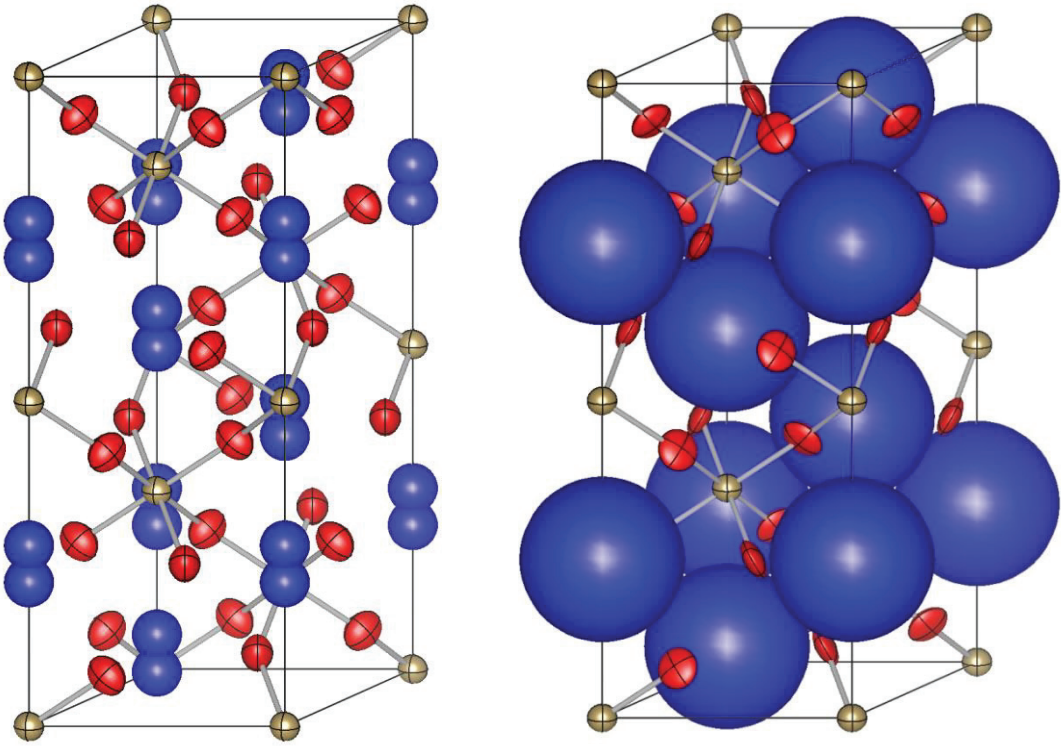

Fig. 4-9 Results of $LiTaO_3$ with two different structure models in the ferroelectric phase at 1050 K; (a) disordered model and (b) displacive model.

The possibility of the Li ion disordered in the paraelectric phase was also examined by bond valence sum (BVS). The BVS is well known as a popular approach to validate an ionic valence of a constituent cation and transport pathways of an ion from the view point of crystal chemistry [86]. The BVS can be calculated by

$$\mathrm{BVS} = \sum_i \left(\frac{R_i - R_0}{B} \right) \tag{4-1}$$

where B is the bond softness, R_i is the interatomic distance and Interatomic distance for transferring one electron from the cation to anion. The BVS of the Li ion were calculated by considering the contribution from the O atoms up to the second nearest neighbor for the Li ion, where the empirical BVS parameters R_0 =1.466(3) and B = 0.37 provided by Brown et al. were used [87].

Table 4-2 Structural parameters of $LiTaO_3$ at 1050 K.

(a) Paraelectric phase at 1050 K. Space group: $R\bar{3}c$. Lattice parameter: a = 5.23175(8) Å, and c = 13.76475(21). R_{WP} = 4.85%, R_I = 1.33%, and R_F = 1.35% for data with d > 0.458 Å.

Atom	x	y	z	Occupancy	U_{11} or U_{iso}	U_{22}	U_{33}	U_{12}	U_{23}	U_{13}
Li	0	0	0.278(1)	0.5	4.23(56)	-	-	-	-	-
Ta	0	0	0	1	1.50(1)	= U_{11}	1.41(4)	0.744(7)	0	0
O	0.3843(3)	0.3755(3)	0.25	1	1.89(16)	2.77(61)	2.57(65)	1.39(31)	-0.44(51)	-0.22(25)

(b) Paraelectric phase (1050 K) with the displacive model. Space group: $R\bar{3}c$. Lattice parameter: a = 5.23175(8) Å, c = 13.76475(21). R_{WP} = 5.036%, R_I = 2.355%, and R_F = 1.846% for data with d > 0.458 Å.

Atom	x	y	z	Occupancy	U_{11} or U_{iso}	U_{22}	U_{33}	U_{12}	U_{23}	U_{13}
Li	0	0	0.25	1	48.2(20)	-	-	-	-	-
Ta	0	0	0	1	1.50(2)	= U_{11}	1.41(4)	0.752(7)	0	0
O	0.06045)	0.3333	0.0833	1	1.73(16)	3.16 (65)	2.58(67)	1.58(33)	-0.21(54)	-0.10(27)

Figure 4-10 shows the evaluated BVS of the Li ion at (0, 0, z) around z = 0.25. Normally the Li ion may prefer the sites at BVS = +1. However, the values in Fig. 2 are entirely smaller than the ideal ionic valence +1 because of the longer Li-O interatomic distances at high temperature. Adams [88] suggests for close packed ion conductors that ion transport pathways may be detected by finding the bond valence isosurface of minimum valence. We can find two minima of the BVS at z = 0.225 and 0.275 in Fig. 2, which are close to the z-coordinates of the Li ion refined by the Rietveld method in Table I. From the examination of BVS, we have learned that the framework constituted of TaO_3 in the paraelectric structure essentially involves the Li ion disordered at the two sites in the c-axis.

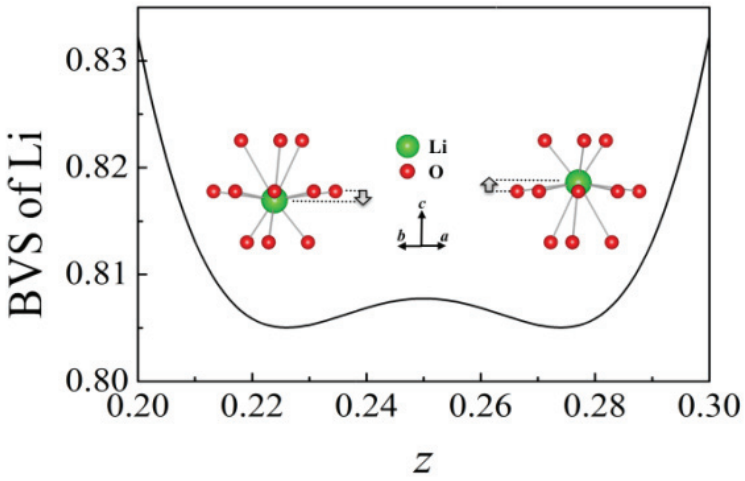

Fig. 4-10 Bond valence sum (BVS) of Li ion at (0, 0, z) around z = 0.25 at 1050 K in paraelectric phase. The framework constituted of TaO_3 in the paraelectric structure of $LiTaO_3$ essentially involves the Li ion disordered at the two sites in the c-axis.

4.3 Charge density study

The electron charge density distributions were visualized by the MEM technique using the structure factors obtained by the Rietveld method. The 3D images of the ferroelectric and paraelectric structures are depicted outside left and right in Fig. 4-11, respectively, and the corresponding 2D maps around the Li atom and their 1D line profiles inside in Fig. 4-11. From the 3D images, it is found that the Li ion is isolated from others, and has ionic chemical bonding character. Although the Li^+ ion has only two electrons, the electron charge density distribution is successfully visualized by SXRD. In the 2D map, the Li ion shows a maximum in the ferroelectric structure, while two maxima in the paraelectric structure in the c-axis. The maximum positions in the 2D maps well coincide with the atomic positions of the Li ion refined by the Rietveld analysis as shown in Table 4-2. From these results, it can be seen that the disordered Li ion along the polar direction at the two sites in the paraelectric phase is ordered at one site in the ferroelectric phase. This is the direct evidence that the phase

transition in $LiTaO_3$ is associated with the order-disorder of the Li ion.

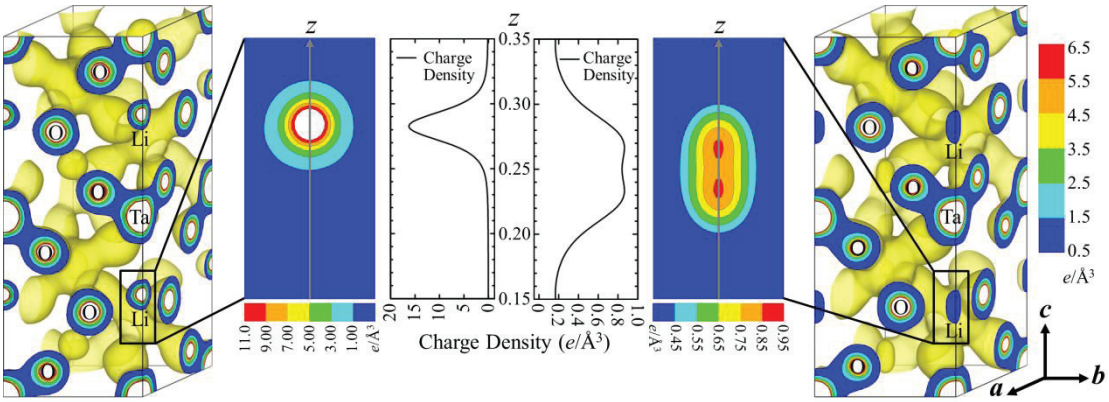

Fig. 4-11 MEM electron charge density distributions of $LiTaO_3$ at 123 K in ferroelectric phase (left) and 1050 K in paraelectric phase (right). The 3D images are depicted outside, and the corresponding 2D maps around the Li ion and their 1D line profiles inside. The equi-charge density surface of the 3D figures is 0.5 e/Å^3. The disordered Li ion in the polar direction at the two sites in the paraelectric phase is ordered at one site in the ferroelectric phase.

4.4 Structures at different temperature

Figure 4-12 shows the Debye Scherrer pattern of $LiTaO_3$ obtained by synchrotron radiation powder diffraction experiments at the temperature from 300 K to 1150 K. By integrating the intensities of these diffraction images with a width of 2.5 mm with respect to the diffraction angle 2θ, we made one dimension, and Rietveld analysis was carried out.

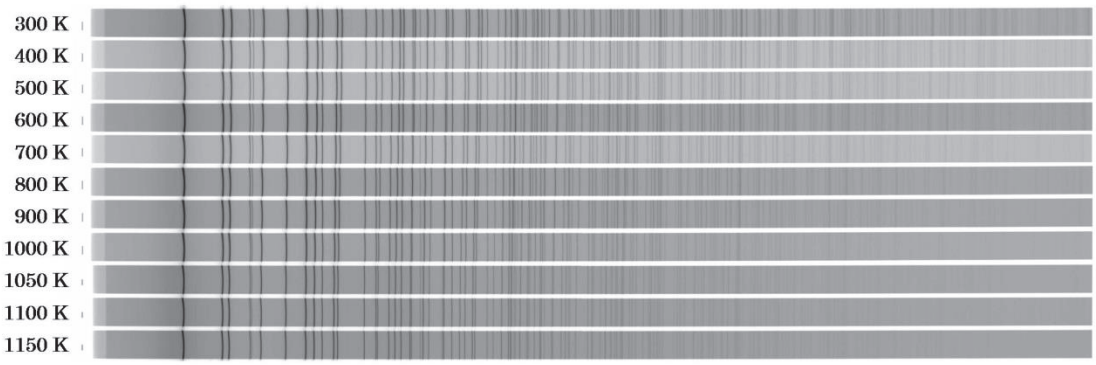

Fig. 4-12 Debye Scherrer patterns of $LiTaO_3$ ranging from 300 K to 1150 K recorded on the imaging plate.

Table 4-3 ~ 4-13 shows the analysis range, structural parameters, and reliability factor values of Rietveld analysis at each temperature, and Figure 4-13 - 4-23 shows the profile fitting result of Rietveld analysis. In the structure analysis, I assumed the space group of $R3c$ for the data from 300 to 960 K as the ferroelectric phase, while $R\bar{3}c$ for the data from 1000 K and above as the paraelectric phase.

Table 4-3 Structural parameters of 300 K. a = 5.14951(1) Å, c = 13.77265(4) Å. Analysis range: d > 0.50 Å (2θ<59.85). R_{WP} = 4.291%, R_I = 1.741%, R_F = 1.301%.

Atom	x	y	z	Occupancy	U [Å^2]
Li	0	0	0.2812(8)	1	0.012(2)
Ta	0	0	0	1	0.00404(3)
O	0.0523(4)	0.344(1)	0.0692(2)	1	0.0042(6)

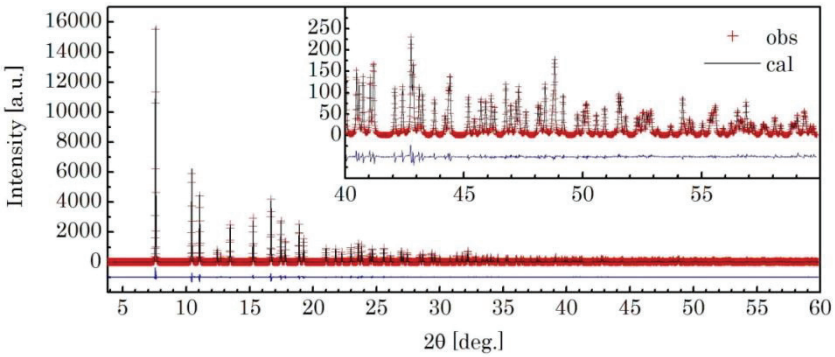

Fig. 4-13 profile fitting result of $LiTaO_3$ at 300 K.

Table 4-4 Structural parameters of $LiTaO_3$ at 400 K. a = 5.15905(1) Å, c = 13.77524(5) Å. R_{WP} = 4.601%, R_I = 2.018%, R_F = 1.895% d > 0.50 Å (2θ < 59.85)

Atom	x	y	z	Occupancy	U [Å^2]
Li	0	0	0.281(1)	1	0.018(3)
Ta	0	0	0	1	0.00487(3)
O	0.0525(5)	0.343(1)	0.0693(3)	1	0.0053(7)

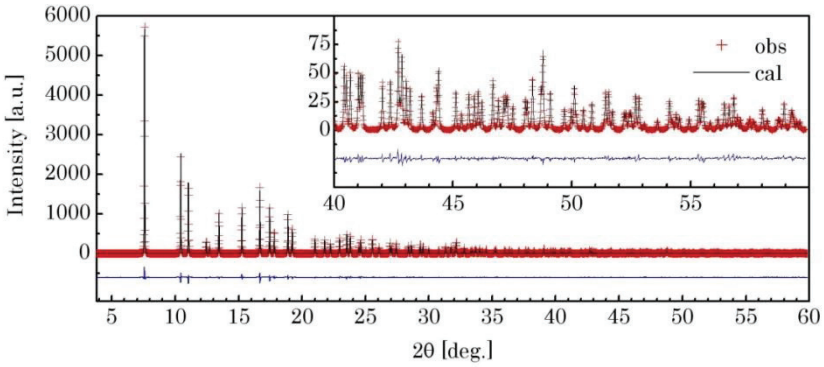

Fig. 4-14 Profile fitting result of $LiTaO_3$ at 400 K.

Table 4-**5** Structural parameters of $LiTaO_3$ at 500 K. a = 5.16776(1) Å, c = 13.77698(5) Å. R_{WP} = 4.447%, R_I = 2.186%, R_F = 2.106%. Analysis range: d > 0.50 Å (2θ < 59.85)

Atom	x	y	z	Occupancy	U [Å^2]
Li	0	0	0.279(1)	0.95	0.020(3)
Li	0	0	0.221(1)	0.05	0.020(3)
Ta	0	0	0	1	0.00592(4)
O	0.0527(5)	0.341(1)	0.0695(3)	1	0.0054(7)

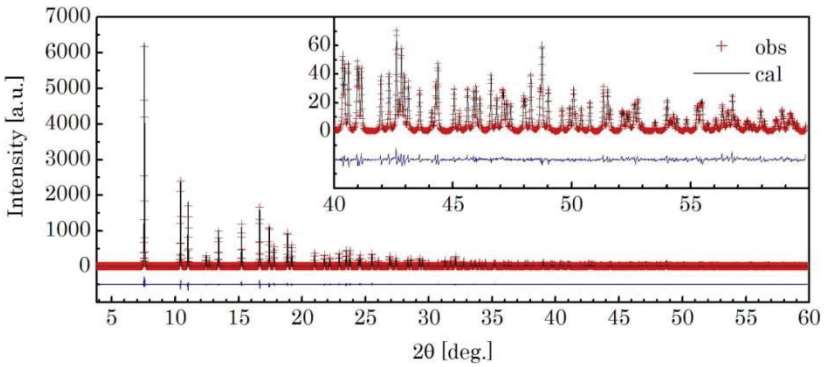

Fig. 4-15 Profile fitting result of $LiTaO_3$ at 500 K.

Table 4-6 Structural parameters of $LiTaO_3$ at 600 K. a = 5.17741(1) Å, c = 13.77824(5) Å. R_{WP} = 4.211%, R_I = 1.822%, R_F = 1.441%. Analysis range: d > 0.50 Å (2θ < 59.85).

Atom	x	y	z	Occupancy	U [Å^2]
Li	0	0	0.277(1)	0.9	0.025(3)
Li	0	0	0.223(1)	0.1	0.025(3)
Ta	0	0	0	1	0.00716(4)
O	0.0550(4)	0.342(1)	0.0706(3)	1	0.0080(7)

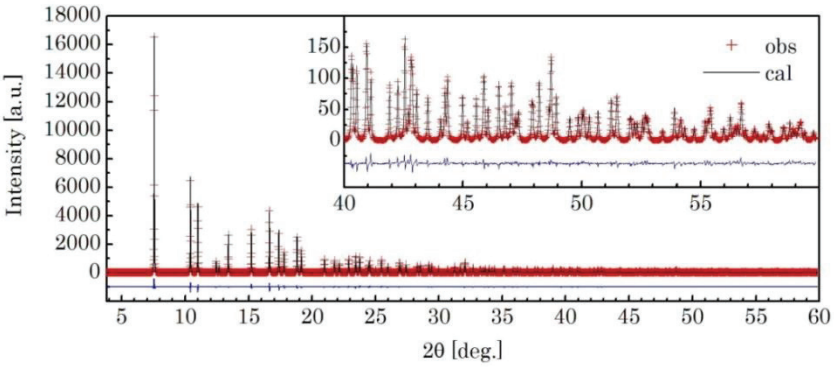

Fig. 4-16 Profile fitting result of $LiTaO_3$ at 600 K.

Table 4-7 Structural parameters of $LiTaO_3$ at 700 K. a = 5.18876(1) Å, c = 13.77781(5) Å. R_{WP} = 4.365%, R_I = 2.159%, R_F = 2.067%. Analysis range: d > 0.50Å (2θ < 59.85).

Atom	x	y	z	Occupancy	U [Å^2]
Li	0	0	0.277(1)	0.9	0.040(5)
Li	0	0	0.223(1)	0.1	0.040(5)
Ta	0	0	0	1	0.00821(5)
O	0.0569(5)	0.341(1)	0.0716(3)	1	0.0078(7)

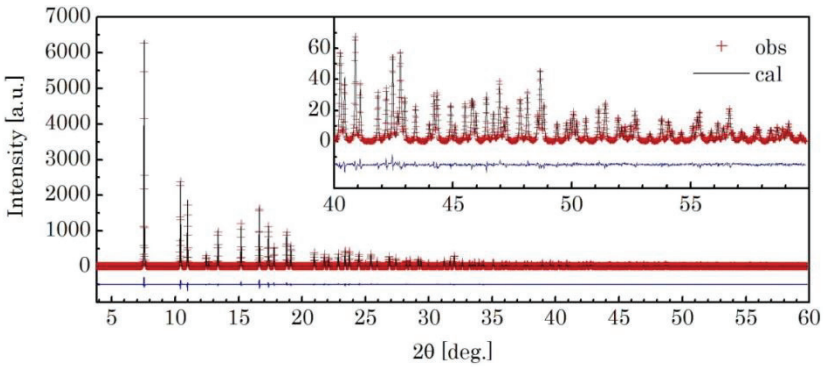

Fig. 4-17 Profile fitting result of $LiTaO_3$ at 700 K.

Table 4-8 Structural parameters of $LiTaO_3$ at 800 K. a = 5.20026(2) Å, c = 13.77431(7) Å. R_{WP} = 5.072%, R_I = 2.070%, R_F = 1.635%. Analysis range: d > 0.50 Å (2θ < 59.85).

Atom	x	y	z	Occupancy	U [Å^2]
Li	0	0	0.280(1)	0.82	0.032(5)
Li	0	0	0.220(1)	0.28	0.032(5)
Ta	0	0	0	1	0.01009(6)
O	0.0603(5)	0.346(2)	0.0722(4)	1	0.010(1)

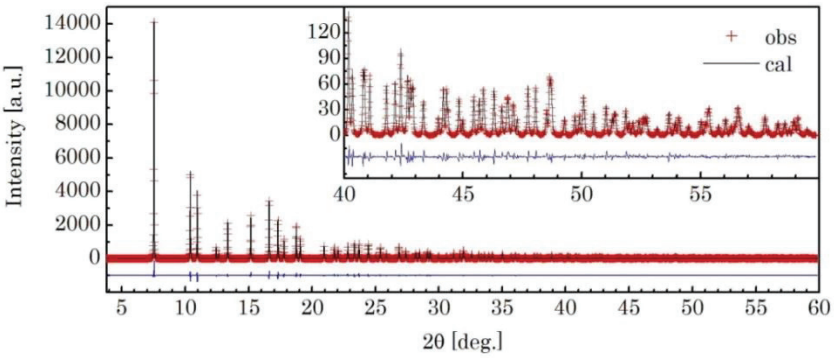

Fig. 4-18 Profile fitting result of $LiTaO_3$ at 800 K.

Table 4-9 Structural parameters of $LiTaO_3$ at 900 K. a = 5.21312(2) Å, c = 13.76906(7) Å. R_{WP} = 4.988%, R_I = 2.033%, R_F = 1.706%. Analysis range: d > 0.50Å (2θ < 59.85).

Atom	x	y	z	Occupancy	U [Å^2]
Li	0	0	0.277(1)	0.82	0.034(5)
Li	0	0	0.223(1)	0.28	0.034(5)
Ta	0	0	0	1	0.01189(7)
O	0.0636(5)	0.349(2)	0.0751(5)	1	0.011(1)

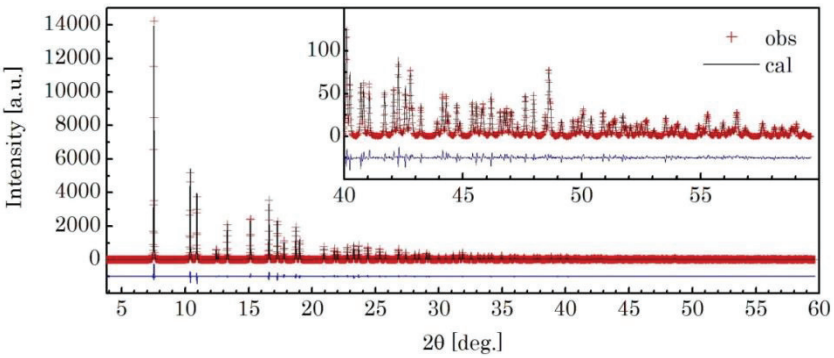

Fig. 4-19 Profile fitting result of $LiTaO_3$ at 900 K.

Table 4-10 Structural parameters of $LiTaO_3$ at 1000 K. a = 5.22624(2) Å, c = 13.76197(7) Å. R_{WP} = 4.973%, R_I = 1.983%, R_F = 1.525% Analysis range: d > 0.60 Å (2θ < 49.25).

Atom	x	y	z	Occupancy	U [Å^2]
Li	0	0	0.221(1)	0.5	0.048(7)
Ta	0	0	0	1	0.01352(8)
O	0.6094(5)	0	0.25	1	0.0163(8)

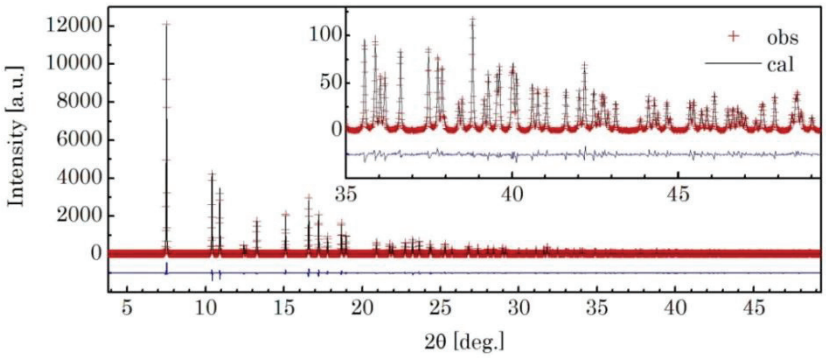

Fig. 4-20 Profile fitting result of $LiTaO_3$ at 1000 K.

Table 4-11 Structural parameters of $LiTaO_3$ at 1050 K. a = 5.23263(1) Å, c = 13.76466(4) Å. R_{WP} = 2.691%, R_I = 1.454%, R_F = 1.296%. Analysis range: d > 0.60 Å (2θ < 49.25)

Atom	x	y	z	Occupancy	U [Å^2]
Li	0	0	0.2208(8)	0.5	0.045(4)
Ta	0	0	0	1	0.01414(5)
O	0.6109(3)	0	0.25	1	0.0193(5)

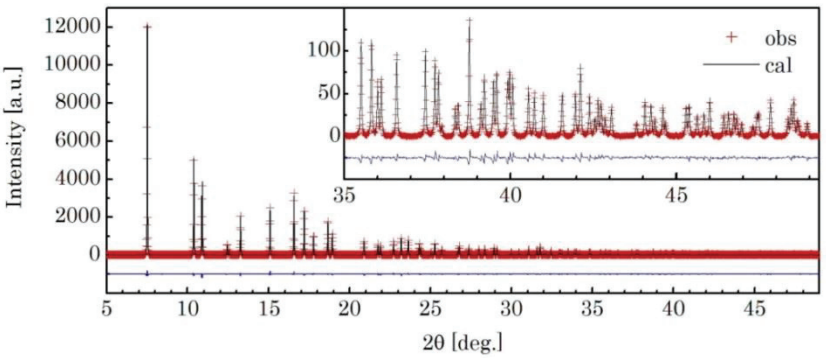

Fig. 4-21 Profile fitting result of $LiTaO_3$ at 1050 K.

Table 4-12 Structural parameters of $LiTaO_3$ at 1100 K. a = 5.23766(1) Å, c = 13.76723(4) Å. R_{WP} = 2.636%, R_I = 1.556%, R_F = 1.270%. Analysis range: d > 0.60 Å (2θ < 49.25).

Atom	x	y	z	Occupancy	U [Å^2]
Li	0	0	0.219(1)	0.5	0.058(4)
Ta	0	0	0	1	0.01457(5)
O	0.6099(3)	0	0.25	1	0.0196(5)

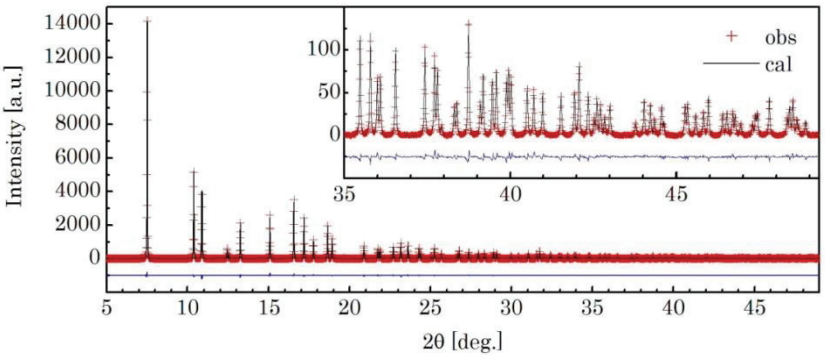

Fig. 4-22 Profile fitting result of $LiTaO_3$ at 1100 K.

Table 4-13 Structural parameters of $LiTaO_3$ at 1150 K. a = 5.24277(1) Å, c = 13.76968(4) Å. R_{WP} = 2.790%, R_I = 1.559%, R_F = 1.341%. Analysis range: d > 0.60 Å (2θ < 49.25).

Atom	x	y	z	Occupancy	U [Å^2]
Li	0	0	0.219(1)	0.5	0.055(4)
Ta	0	0	0	1	0.01496(5)
O	0.6100(4)	0	0.25	1	0.0205(5)

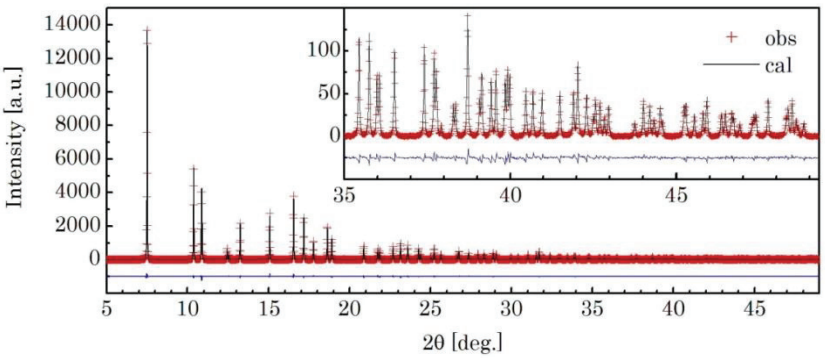

Fig. 4-23 Profile fitting result of $LiTaO_3$ at 1150 K.

The temperature dependence of the difference in occupancy of the Li ion and the positions of the Li ion are shown in Fig. 4-24. In the paraelectric phase above T_C, the Li ion is disordered at the two sites with the same occupancy of 0.5. In the ferroelectric phase below T_C, the Li ion is gradually ordered at the one site changing the occupancy with decreasing temperature, and fully ordered at around 400 K. The z-coordinates of the disordered sites of the Li ion are almost unchanged in the entire temperature range.

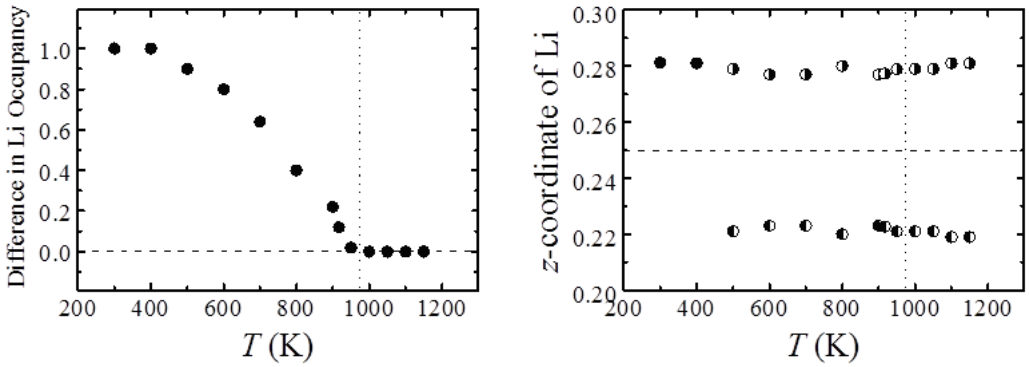

Fig. 4-24 (a) Difference in occupancy of the Li ion at two sites and (b) the positions of the Li ion.

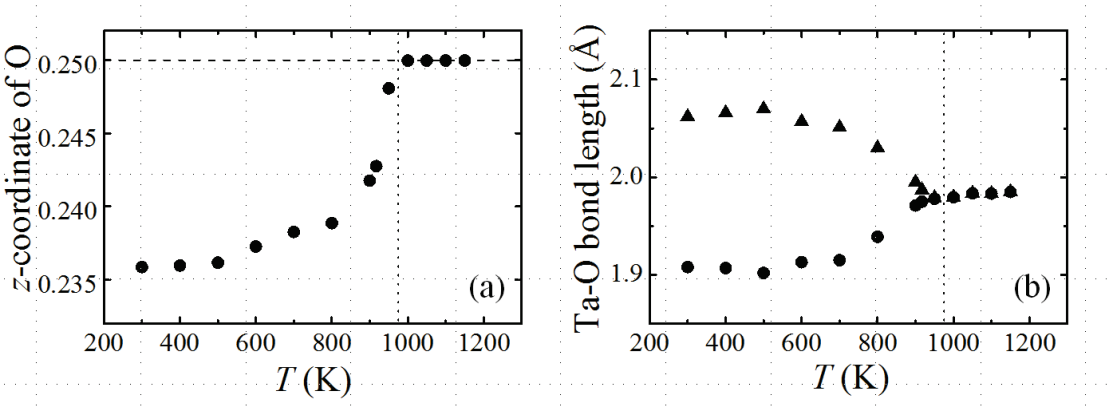

Fig. 4-25 (a) z-coordinate of O atom and (b) Ta-O bond length as functions of temperature.

Associated with the progress of ordering of the Li ion, the atomic position of O gradually changes below T_C as show in Fig. 4-25 (a), which results in the gradual changes of the Ta-O bond length below T_C. No discontinuous change in the bond length

is seen at T_C as show in Fig. 4-25 (b), although Boysen et al. suggest that the Nb-O bond length in $LiNbO_3$ discontinuously changes at T_C.[61] We presume that few data points measured in the vicinity of T_C in the experiment by Boysen et al. give rise to the discrepancy.

4.5 Spontaneous polarization

Calculation of the spontaneous polarization magnitude of $LiTaO_3$ was carried out using a point charge model in which each atom exists in a formal valence. Using that model the spontaneous polarization P_S can be calculated by

$$P_S = \frac{e}{V}\sum_j N_j q_j \Delta r_j \ , \qquad (4\text{-}1)$$

where V is the unit lattice volume, N is the number of atoms per unit lattice volume, q is the valence of each atom, and Δr is the displacement amount of each atom. By this P_S calculation, the contribution of ion polarization can be predicted mainly. Using this formula, the spontaneous polarization magnitudes of the tetragonal, orthorhombic and rhombohedral phases of $LiTaO_3$ were calculated as K^+, Ta^{5+}, and O^{2-}.

The spontaneous polarization P_S of $LiTaO_3$ evaluated from the crystal structure based on the point charge model is shown in Fig. 4-26, where the formal charge of each ion is assumed, and the origin of the ionic displacement toward the polar direction is at the Ta site. The evaluated P_S which is indicated by solid circles in the figure gradually increases at T_C with decreasing temperature. The temperature dependence is similar to that measured by Iwasaki et al.[89]. The evaluated P_S in this study is 48.6 $\mu C/cm^2$, which is almost the same as the observed P_S [38]. Therefore, we consider that P_S of $LiTaO_3$ is mainly caused by the displacement of ions, that is, the ionic polarization, and the contribution from the electronic polarization to P_S is little.

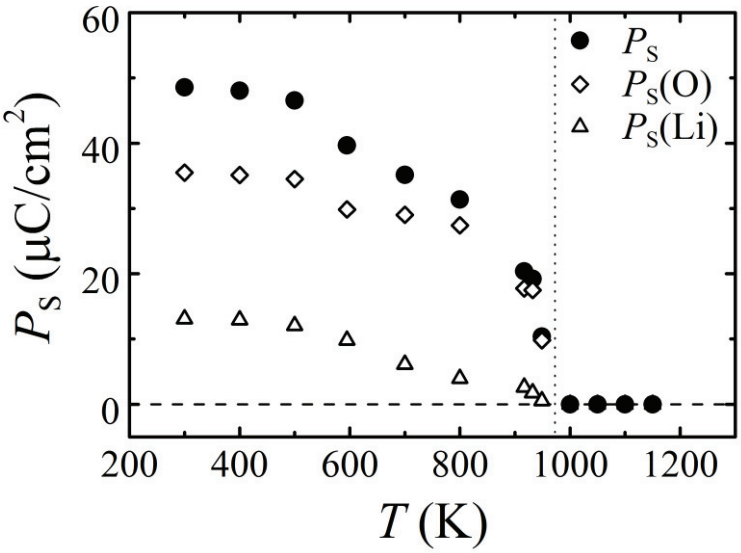

Fig. 4-26 Spontaneous polarization evaluated from the crystal structure of $LiTaO_3$ as a function of temperature based on the point charge model. The contributions from O and Li to the total spontaneous polarization P_S (solid circles) are plotted by open triangles and diamonds as P_S(O) and P_S(Li), respectively. The origin of the ionic displacement is at the Ta site.

4.6 Lattice strain

The temperature dependences of the lattice parameters *a* and *c* based on the hexagonal unit cell, the volume of unit cell, and the spontaneous lattice strains are indicated in Fig. 4-27. The lattice parameter *a* decreases with decreasing temperature, and *c* exhibits a negative thermal expansion in the wide temperature range below T_C. The deviated magnitude from the broken line corresponds to the spontaneous lattice strain in the ferroelectric phase. The lattice strain ε_1 in the *a*-axis is negative in the ferroelectric phase, while the lattice strain ε_3 in the *c*-axis is positive. The volume of unit cell, hence, results in decreasing monotonically with decreasing temperature in the entire temperature range, and no significant abnormally is seen at T_C. The temperature dependence of ε_3 in Fig. 4-27(d) is similar to those of the occupancy of the Li ion in Fig. 4-24 (a) and P_S in Fig. 4-25 at a glance.

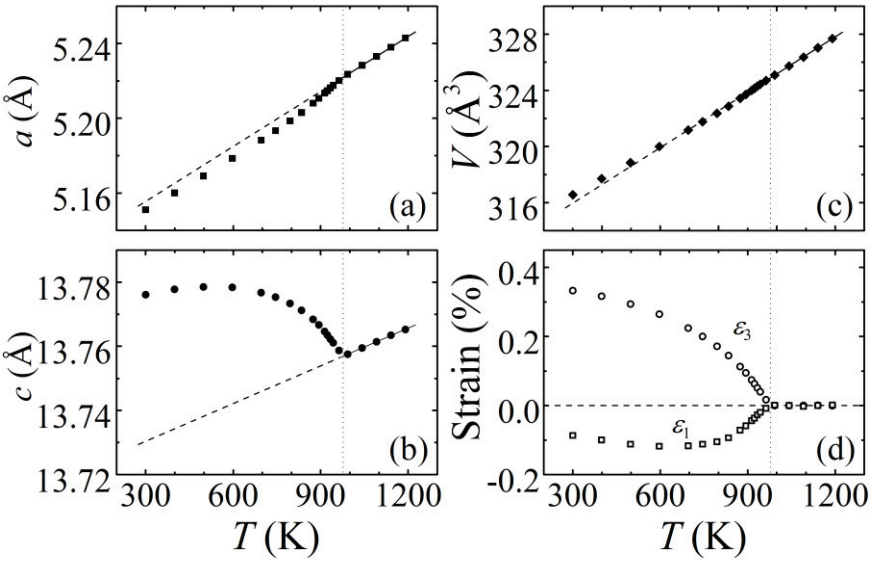

Fig. 4-27 Temperature dependence of structural parameters and spontaneous lattice strain; (a) lattice parameter *a*, (b) *c*, (c) hexagonal unit cell volume, and (d) lattice strains ε_1 in *a*-axis and ε_3 in *c*-axis.

Chapter 5

Structure of $LiNbO_3$ at 123 K and comparison with $LiTaO_3$

5.1 Rietveld refinement of $LiNbO_3$ at 123 K

The Debye Scherrer patterns of the low-angle and high-angle data of $LiNbO_3$ (123 K, rhombohedral phase with space group *R*3*c*) in the ferroelectric phase obtained by synchrotron radiation powder diffraction experiment is shown in Fig. 5-1. Precise structural analysis of $LiNbO_3$ was performed using this this data.

Fig. 5-1 Debye-Scherrer patterns of $LiNbO_3$ at 123 K recorded on the imaging plate.

As mentioned before, the contribution from the Li ion to the most intense diffraction peak of $LiNbO_3$ is about 0.3%, we employed the similar way as $LiTaO_3$ to know the approximate position of the Li ions at the initial stage of the refinement. An isotropic displacement parameter was assumed for the Li ion while anisotropic displacement parameters for the Nb and O atoms. The refined structure parameters are summarized in Table 5-1, with the atomic coordinates of the Nb atom fixed at the original point (0, 0, 0). The atomic displacement parameters *U* of the Li ion and the O atom are almost the same for the materials, respectively, which indicate the similar environments around the Li ion and O atom in the two materials, respectively. However, *U* parameters of the Nb atom are slightly larger than those of the Ta atom.

Table 5-1 Structural parameters of $LiNbO_3$ at 123 K obtained by Rietveld analysis. Space group: *R*3*c*. a = 5.13761(1) Å, c = 13.84970(4) Å, V = 316.587(2) Å^3. R_{WP} = 1.07%, R_I = 3.11%, R_F = 2.43%.

Atom	x	y	z	U_{11} or U_{iso} [10^{-2} Å^2]	U_{22} [10^{-2} Å^2]	U_{33} [10^{-2} Å^2]	U_{12} [10^{-2} Å^2]	U_{23} [10^{-2} Å^2]	U_{13} [10^{-2} Å^2]
Li	0	0	0.2810(3)	0.946(61)	-	-	-	-	-
Nb	0	0	0	0. 172(3)	= U_{11}	0. 13(1)	= U_{11}/2	0	0
O	0.3805(3)	0.3753(3)	0.2295(1)	0. 296(38)	0.36(13)	0.46(13)	0.21(8)	0.024(92)	-0.049(97)

The result of the Rietveld profile fitting of $LiNbO_3$ in the ferroelectric phase at 123 K is shown in Fig. 5-2 for the 2θ range less than 60° (d > 0.3550 Å).

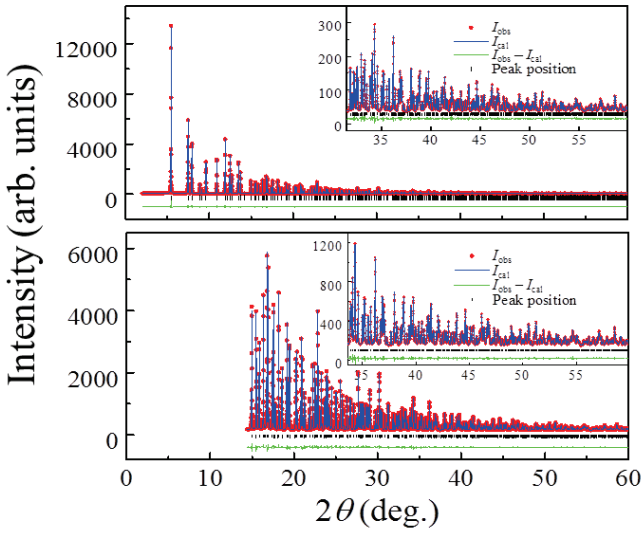

Fig. 5-2 Fitting diffraction pattern of $LiNbO_3$ at 123 K.

As a result of crystal structure analysis, the thermal vibration amplitude U_{Nb} of Nb in $LiNbO_3$ at 123 K is 1.549 10^{-2} Å^2, and the thermal oscillation amplitude U_{Ta} of Ta of $LiTaO_3$ is 0.894 10^{-2} Å^2. In order to consider the influence of mass on thermal vibration, the vibration amplitude was calculated from the mass ratio of Nb atom and Ta atom. Considering harmonic oscillation, the two constants k are the same. Consider the following differential equation as harmonic oscillation.

In case

$$m\frac{d^2x}{dt^2} = -kx, \tag{5-1}$$

the solution of this differential equation is

$$x = a\sin(\sqrt{\frac{k}{m}}t + \delta), \tag{5-2}$$

where a is the amplitude of this oscillation, and δ is the phase at t = 0. The mass m_{Nb} of Nb atom was 92.906 g / mol and the mass m_{Ta} of Ta atom was 180.948 g / mol, and the ratio a_{Nb} / a_{Ta} of the amplitudes of them was calculated to be a_{Nb} / a_{Ta} = 1.396. This value a little smaller than the value of the thermal vibration amplitude ratio $(U_{Nb}/U_{Ta})^{1/2}$ = 1.21. Since the ionic radii of Nb and Ta are almost the same and the lattice constants are also almost the same, the difference between the thermal oscillation amplitude cannot be only attributed to the masses of Nb and Ta, which indicates the constant *k* of $LiNbO_3$ is larger than that of $LiTaO_3$. This may means the bond between Nb and O is harder than that between Ta and O, which will be discussed later.

5.2 Spontaneous polarization at 123 K

In the last chapter, the temperature-dependence spontaneous polarization calculated by point charge model using the displacement of the Li and O atoms related to the Ta atom has been discussed. Although it is convenient to calculate the spontaneous polarization using the results of Rietveld refinement, the mothed cannot reveal the emergence of the spontaneous polarization because the $LiNbO_3$-type materials have layered structure with the Li and Ta atoms inserted in the O-layers with the same distances, which are 1/6 of the lattice parameter *c* and the spontaneous polarization arises from the displacement of the cations related to the O-layers.

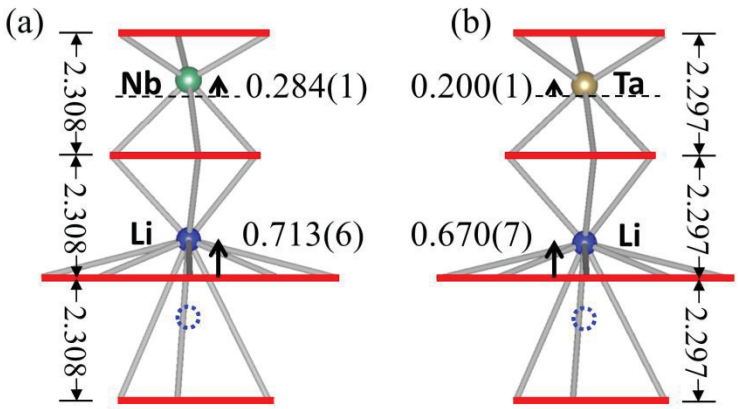

Fig. 5-3 Schematic views of crystal structures of (a) $LiNbO_3$ and (b) $LiTaO_3$ at 123 K in ferroelectric phase. The unit of all the values is Å. The red lines indicate the O layers. The atomic shifts of the Li ion and the Nb(Ta) atom at 123 K are indicated by arrows. Another Li ion site disordered in the paraelectric phase is indicated by a broken circle.

The schematics of the crystal structures for $LiNbO_3$ and $LiTaO_3$ are shown in Fig. 5-3. The red lines stand for the O layers. The distances between the O layers are 2.308 and 2.297 Å for $LiNbO_3$ and $LiTaO_3$, respectively. The dash lines, which are in the middle of the O layers, represent the positions of the Nb and Ta atom in the paraelectric phases, respectively. The average positions of the Li ion in the paraelectric phases for both crystals are located in the long O layers, and another Li ion site disordered in the paraelectric phase is indicated by broken circle. The small arrows indicate the displacements of all cations in both materials. The entire cations in the ferroelectric phases shift upward compared to the O layers in both materials, which give rise to spontaneous polarization upward along the *c*-axis.

The ionic polarizations evaluated from the shifts of the cations based on the point charge model using Equation 4-1 are shown as Table 4-2. The total calculated polarizations for $LiNbO_3$ and $LiTaO_3$ are 64.7 and 50.9 μC/cm, respectively. These values are both more than 90% of the measured spontaneous polarization P_S [38,40]. The spontaneous polarization is consist of the ionic polarization and the electronic polarization, so the contribution from the ionic polarization to the P_S is significantly

high in the case of $LiNbO_3$ and $LiTaO_3$, which provides a great contrast to the case of $PbTiO_3$ with the large electronic polarization by a lone electron pair of the Pb^{2+} ion [90]. Therefore, we consider that the P_S of $LiNbO_3$ and $LiTaO_3$ are mainly caused by the shift of ions, that is, the ionic polarization, and the contribution from the electronic polarization to the P_S is not significant.

Table 5-2 Spontaneous polarization calculated by the point charge model for $LiNbO_3$ and $LiTaO_3$.

Material	Atom	Formal charge	Δr [Å]	Contribution to P_S [μC/cm^2]	Total P_S [μC/cm^2]	Measured P_S [μC/cm^2]
$LiNbO_3$	Li	+1	0.713(6)	21.6	65.7	71
	Nb	+5	0.284(1)	43.1		
$LiTaO_3$	Li	+1	0.670(7)	20.4	50.9	55
	Ta	+5	0.200(1)	30.5		

On the other hand, the contribution to the ionic polarization of $LiNbO_3$ from the Nb atom is 43.1 μC/cm^2, which is much larger than 30.5 μC/cm^2 from the Ta atom in $LiTaO_3$, while the contribution to the ionic polarization from the Li ion is almost the same as 21.6 and 20.4 μC/cm^2 for $LiNbO_3$ and $LiTaO_3$, respectively. Hence, we consider that the larger atomic shift of the Nb atom plays an important role in the emergence of larger P_S in $LiNbO_3$.

5.3 Charge density distribution of $LiNbO_3$ and $LiTaO_3$ at 123 K

The electron charge density distributions were visualized by the MEM technique using the structure factors obtained by the Rietveld method. The 3D electron charge

density distributions of stoichiometric $LiNbO_3$ and $LiTaO_3$ in the ferroelectric phase are shown in Fig. 5-4 along with the 1D electron charge density profiles of the constituent ions and atoms in the polar direction. The 3D images clearly reveal that the Nb-O and Ta-O bonds show covalent character, while the Li ion is isolated from others to show ionic character. The high-quality SXRD data enable us to visualize the electron charge density distributions of the Li^+ ion accurately in both the materials, although there are only two electrons around the Li^+ ion. Each peak position of the 1D profile well agrees with the *z*-coordinate of each atom in Table I. It looks that the Li ion in $LiNbO_3$ is fully ordered at one site in the ferroelectric phase at low temperature 123 K as well as in the case of $LiTaO_3$. The corresponding 1D charge density profiles are very similar with each other. However, 1D profiles of the Li ion are significantly broader than those of the Nb, Ta and O atoms due to the high mobility still at this temperature.

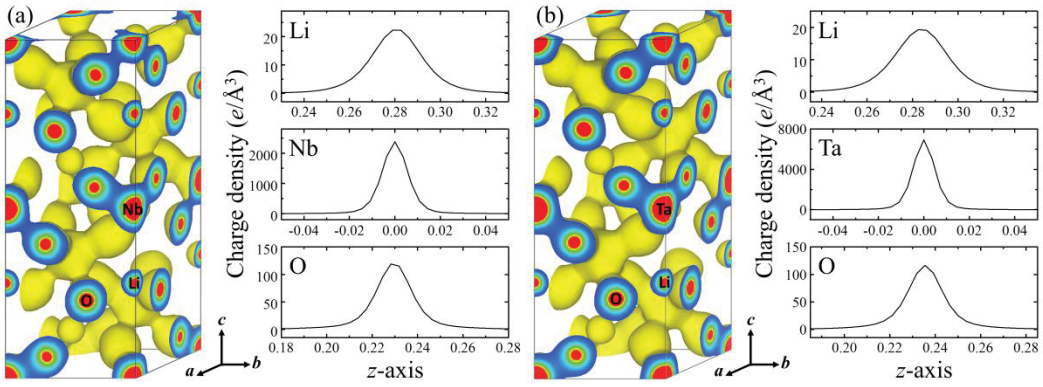

Fig. 5-4 3D electron charge density distributions of (a) $LiNbO_3$ and (b) $LiTaO_3$[24] at 123 K in hexagonal unit cell with 1D electron charge density profile of constituent ion and atoms along *c*-axis . The equi-charge density surface of the 3D figures is 0.5 $e/Å^3$.

5.4 Relationship between Nb(Ta)-O bond length, charge density and T_C

Figure 5-5 shows the crystal structures of the Nb-O and Ta-O oxygen octahedra in $LiNbO_3$ and $LiTaO_3$, respectively, indicated by the ball-and-stick images and the 3D images of electron charge density distributions. The Nb and Ta atoms are surrounded by the six O atoms, respectively. The O atoms were labeled as O1 and O2 atoms in the figure for convenience although the crystallographically equivalent O atom is only one in the unit cell. The three Nb(Ta)-O1 bonds with the same bond length and another three Nb(Ta)-O2 bonds also with the same bond length can be seen in Fig. 5-6. The formers are shorter than the latters. The minimum electron charge density ρ_{min}(Nb(Ta)-O1) on the Nb(Ta)-O1 short bond is higher than the ρ_{min}(Nb(Ta)-O2) on the Nb(Ta)-O2 long bond. Hence, it can be considered that the short bonding is basically harder than the long one.

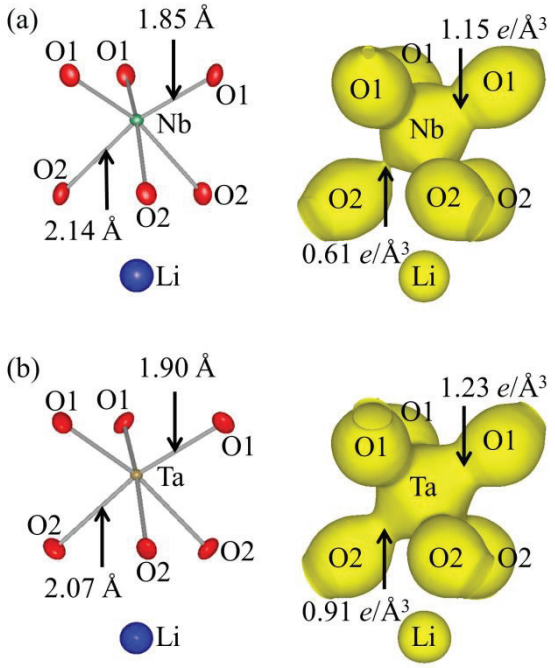

Fig. 5-5 Crystal structures of Nb-O and Ta-O oxygen octahedra in (a) $LiNbO_3$ and (b) $LiTaO_3$, respectively, indicated by ball-and-stick images and 3D images of electron charge density distributions at 123 K. The thermal ellipsoids in the ball-and-stick images are drawn at the 99% probability level.

Regarding the comparison of the corresponding bond length between $LiNbO_3$ and $LiTaO_3$, the Nb-O1 bond is shorter than the Ta-O1 bond, while the Nb-O2 bond is

longer than the Ta-O2 bond in the oxygen octahedra, because of the larger atomic shift of the Nb atom toward the O1 atoms in the oxygen octahedron of $LiNbO_3$. The Nb-O octahedron is more distorted than the Ta-O octahedron. In this case, for example, we may suppose that the Nb and O1 atoms with the shortest interatomic distance are well hybridized to form the strong covalent bonding, and the ρ_{min}(Nb-O1) should be higher than the ρ_{min}(Ta-O1). However, the relation is opposite as shown in Fig. 5-5. We consider that this is due to the valence electrons distribution apparently overlapping with the core electrons distribution on the bonds in the figure. The effect from the Ta atom with much more core electrons is more crucial than that from the Nb atom.

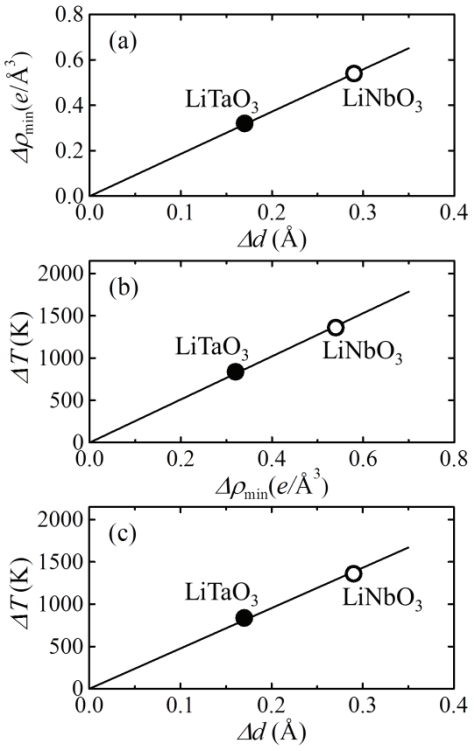

Fig. 5-6 Relationships between bond length, electron charge density on bond and Curie temperature T_C revealed in $LiNbO_3$ family crystals. (a) $\Delta\rho_{min}$ vs Δd, (b) ΔT vs $\Delta\rho_{min}$ and (c) ΔT vs Δd.

Hence, in order to eliminate the effect from the inner core electrons to the whole electron charge density distribution as much as possible on the bonds, we propose an indicator, the difference of the minimum electron charge density $\Delta\rho_{min}$ =

ρ_{min}(Nb-O1) − ρ_{min}(Nb-O2) and ρ_{min}(Ta-O1) − ρ_{min}(Ta-O2) for $LiNbO_3$ and $LiTaO_3$, respectively. In Fig. 5-6(a), the charge densities $\Delta\rho_{min}$ of $LiNbO_3$ and $LiTaO_3$ are plotted as a function of the difference of the bond length $\Delta d = d$(Nb-O2) − d(Nb-O1) and d(Ta-O2) − d(Ta-O1), respectively. It can be seen that the two plots are on the same line through the zero point, which means that the $\Delta\rho_{min}$ of these $LiNbO_3$ family crystals can be scaled with Δd. We can estimate the value of $\Delta\rho_{min}$ from that of Δd.

In Fig. 5-6(b), the temperature differences $\Delta T = T_C - T$ of $LiNbO_3$ and $LiTaO_3$ are plotted as a function of $\Delta\rho_{min}$, where T_C = 1480 and 960 K for $LiNbO_3$ and $LiTaO_3$, respectively, and T = 123 K at which these experiments were done. In this figure, we can also see an almost linear relation through the zero point between the charge density on the bond and the T_C of the $LiNbO_3$ family crystals. This relation suggests that the high T_C material comes from the material with a large lattice distortion of the oxygen octahedron, and the T_C of the material is strongly related to the covalency. The crystal orbital overlap population analyses for $LiNbO_3$ and $LiTaO_3$ by Toyoura et al. suggest that the Nb-O bond formed by the Nb4*d*-O2*p* hybridized orbitals has relatively large covalency compared to the Ta-O bond with the Ta5*d*-O2*p* hybridization [56]. We consider that the results of the theoretical studies and this experimental studies can be understood intuitively from the valence electron configuration of the Nb atom with one more *d*-electron in $LiNbO_3$ compared with that of the Ta atom in $LiTaO_3$; Nb: [Kr]$4d^4 5s$, Ta: [Xe]$4f^{14} 5d^3 6s^2$. It is supposed that there are clear relationships between the covalency of the crystal and the physical properties such as T_C in general for ferroelectric oxides.

The most impressive result is obtained from Fig. 5-6(c). We can estimate the absolute T_C of the $LiNbO_3$ family crystals from their structural data using the relation between Δd and ΔT in the figure. Note that the plots of Δd vs. ΔT are shown in Fig. 5-6(c) as a universal relation through the origin zero rather than those of Δd vs. T_C. We propose that the ΔT is the most important indicator of the temperature when we evaluate the lattice distortion. In these $LiNbO_3$ family crystals, the magnitude of the

lattice distortion indicated by Δd are governed by the temperature difference ΔT. Similar relationships can be seen in perovskite-type ferroelectrics, such as $PbTiO_3$ and $BaTiO_3$ [17,91]. Figure 5-6(c) provides an apparent experimental evidence that the T_C of materials with highly distorted oxygen octahedron is fairly high if we compare the structures at the same temperature.

Chapter 6

Conclusion

In this study, electron charge density distributions have been visualized in stoichiometric $LiNbO_3$ and $LiTaO_3$ by synchrotron radiation X-ray powder diffraction (SXRD) to adduce the conclusive evidence on the mechanism of ferroelectric phase transition and the origin of the large difference between the Curie temperatures.

From the charge density images of $LiTaO_3$ at 123 K and 1050 K, it is found that the Li ion is isolated from others, and has ionic chemical bonding character. The Li ion shows one electron density maximum in the ferroelectric structure, while two maxima in the paraelectric structure in the *c*-axis. It can be concluded that the disordered Li ion along the polar direction at the two sites in the paraelectric phase is ordered at one site in the ferroelectric phase. This is the direct evidence that the phase transition in $LiTaO_3$ is associated with the order-disorder of the Li ion.

In the paraelectric phase above T_C, the Li ion is disordered at the two sites with the same occupancy of 0.5. In the ferroelectric phase below T_C, the Li ion is gradually ordered at the one site changing the occupancy with decreasing temperature, and fully ordered at around 300 K. The *z*-coordinates of the disordered sites of the Li ion are almost unchanged in the entire temperature range. Associated with the progress of ordering of the Li ion, the atomic position of O gradually changes below T_C, which results in the gradual changes of the Ta-O bond length below T_C. No discontinuous change in the bond length is seen at T_C.

The evaluated spontaneous polarization P_S by the point charge model gradually increases below T_C with decreasing temperature. The P_S evaluated from the crystal structure of $LiNbO_3$ and $LiTaO_3$ are almost the same as the result of electronic measurement respectively. The main contribution to the P_S of $LiNbO_3$ and $LiTaO_3$ is from the ionic polarization, and the contribution from the electronic polarization is little.

The contribution to the ionic polarization of $LiNbO_3$ from the Nb atom is 43.1 $\mu C/cm^2$, which is much larger than 30.5 $\mu C/cm^2$ from the Ta atom in $LiTaO_3$ at 123 K when the position of the O atom is assumed as an origin. The larger atomic shift of the Nb atom is considered to plays an important role in the emergence of larger P_S in $LiNbO_3$.

The lattice parameter a decreases with decreasing temperature, and c exhibits a negative thermal expansion in the wide temperature range below T_C. The lattice strain ε_1 on the a-axis is negative in the ferroelectric phase, while the lattice strain ε_3 on the c-axis is positive. The volume of unit cell, hence, results in decreasing monotonically with decreasing temperature in the entire temperature range, and no significant abnormally is seen at T_C.

The electron charge densities $\Delta\rho_{min}$ of $LiNbO_3$ and $LiTaO_3$ as a function of the difference of the bond length Δd are on the same line through the origin zero, which means that the $\Delta\rho_{min}$ of these $LiNbO_3$ family crystals can be scaled with Δd, and we can estimate the value of $\Delta\rho_{min}$ from that of Δd. The temperature differences $\Delta T = T_C - T$ of $LiNbO_3$ and $LiTaO_3$ as a function of $\Delta\rho_{min}$ have an almost linear relation through the origin zero. This relation suggests that the high T_C material comes from the material with a large lattice distortion of the oxygen octahedron, and the T_C of the material is strongly related to the covalency. It is demonstrated that there are clear relationships between the covalency of the crystal and the materials properties such as T_C in ferroelectric oxides.

The plots of Δd vs. ΔT have a universal relation through the origin zero. It is proposed that the ΔT is the most important indicator of the temperature when we evaluate the lattice distortion. In these $LiNbO_3$ family crystals, the magnitude of the lattice distortion indicated by Δd is governed by the temperature difference ΔT. It is an apparent experimental evidence that the T_C of materials with highly distorted oxygen octahedron is fairly high if we compare the structures at the same temperature.

Acknowledgment

First, I would like to give special appreciation to my supervisor Prof. Yoshihiro Kuroiwa, who allowed the opportunities for me to study in such a favorable environment and participate in pioneering research on the structure of $LiNbO_3$-type ferroelectrics. I would like to express my grateful gratitude to Prof. Chikako Moriyoshi especially. During my doctoral period, his patient and intellectual guidance enlightened me a lot and motivated me to promote my scientific research. The helpful advice, support, and friendship from Prof. Moriyoshi are not only precious to my academic level but to my daily life and personality as well. I also would like to appreciate Dr. Eisuke Magome who offered me valuable comments and suggestions with my research as well as concern on my life. Their profound knowledge, rigorous academic attitude, keen scientific insight, and the spirit of exploration of science will be the model for me in my whole life.

I would like to acknowledge the great support for synchrotron X-ray powder diffraction experiments from the beamline scientists Dr. Kawaguchi at beamline BL02B2 in SPring-8.

I thank all the staff of physical science office and student support office of graduate school of science for helping me with paper works, information sharing, and scholarship recommendation.

I would like to thank all members of our laboratory: S. Takeda, S. Kawamura, Y. Hoashi, N. Hikiji, M. Ohmoto, Q. Zhao, Y. Nakahira, D. Tsuru, T. Abe, Y. Sunada, Y. Morida, D. Ichihashi, G. Kawamura, Y. Yokoi, T. Suematsu, S. Tsugita, S. Noda, K. Hagura, M. Hattori, M. Muta, H. Shirakuni. As an oversea student, with your help and friendship, I quickly adapted to the environment of learning and living in Japan and kept on well my research work. I enjoyed getting along with you and I will never forget the happy time we worked and play together. I also send my gratitude to Japan student services organization, for providing scholarships for the financial support.

I must say that I feel most honored and happy to be a member of our laboratory and a student of my three teachers.

References:

[1] T. Nakamura, *Ferroelectricity involved Structural Phase Transitions* (Shokabo, Tokyo, 1988) [in Japanese].

[2] Y. Takagi, *Amazing Barium Titanate* (Maruzen Publishing, Tokyo, 1990) [in Japanese].

[3] T. Sakudou, *Solid State Physics —Lattics Dynamics and Dielectric phase Transitions—* (Shokabo, Tokyo, 1993) [in Japanese].

[4] A. V. Hippel, R. G. Breckenridge, F. G. Chesley, and L. Tisza, Ind. Eng. Chem. **38**, 1097 (1946).

[5] B. Wul and I. M. Goldman, C. R. Acad. Sci. USSR **51**, 21 (1946).

[6] S. A. Hayward, S. A. T. Redfern, and E. K. H. Salje, Journal of Physics: Condensed Matter **14**, 10131 (2002).

[7] S. Aoyagi, PhD thesis, Okayama University, 2002 [in Japanese].

[8] J. Harada, J. Cryst. Soc. Jpn **20**, 1 (1978) [in Japanese].

[9] R. Shannon, Acta Crystallogr., Sec. A **32**, 751 (1976).

[10] D. Tsuru, Master thesis, Hiroshima University, 2017 [in Japanese].

[11] W. Zhong and D. Vanderbilt, Phys. Rev. Lett. **74**, 2587 (1995).

[12] G. Pavel and J. B. Andrew, Journal of Physics: Condensed Matter **19**, 176201 (2007).

[13] A. Glazer, Acta Crystallogr., Sec. B **28**, 3384 (1972).

[14] P. Woodward, Acta Crystallogr., Sec. B **53**, 32 (1997).

[15] G. A. Samara, T. Sakudo, and K. Yoshimitsu, Phys. Rev. Lett. **35**, 1767 (1975).

[16] M. E. Lines and A. M. Glass, *Principles and Application of Ferroelectrics and Related Materials* (Oxford, Clarendon, 1977).

[17] Y. Kuroiwa, S. Aoyagi, A. Sawada, J. Harada, E. Nishibori, M. Takata, and M. Sakata, Phys. Rev. Lett. **87**, 217601 (2001).

[18] H. Tanaka, Y. Kuroiwa, and M. Takata, Phys. Rev. B **74**, 172105 (2006).

[19] K. Yoshihiro, F. Hiroshi, S. Akikatsu, A. Shinobu, N. Eiji, S. Makoto, T. Masaki, K. Hitoshi, and A. Tooru, Jpn. J. Appl. Phys. **43**, 6799 (2004).

[20] Y. Mishima, T. Hojo, T. Nishio, H. Sadamura, N. Oyama, C. Moriyoshi, and Y. Kuroiwa, J. Phys. Chem. C **117**, 2608 (2013).

[21] B. T. Matthias and J. P. Remeika, Phys. Rev. **76**, 1886 (1949).

[22] A. A. Ballman, J. Am. Ceram. Soc. **48**, 112 (1965).

[23] F. S. Chen, J. Appl. Phys. **40**, 3389 (1969).

[24] I. P. Kaminow and J. R. Carruthers, Appl. Phys. Lett. **22**, 326 (1973).

[25] V. V. Lemanov and Y. V. Ilisavsky, Ferroelectrics **42**, 77 (1982).

[26] W. S. Wang, Q. Zou, Z. H. Geng, and D. Feng, J. Cryst. Growth **79**, 706 (1986).

[27] A. Holm, Q. Stürzer, Y. Xu, and R. Weigel, Microelectron. Eng. **31**, 123 (1996).

[28] A. A. Ballman, H. J. Levinstein, C. D. Capio, and H. Brown, J. Am. Ceram. Soc. **50**, 657 (1967).

[29] R. L. Barns and J. R. Carruthers, J. Appl. Crystallogr. **3**, 395 (1970).

[30] S. Miyazawa and H. Iwasaki, J. Cryst. Growth **10**, 276 (1971).

[31] J. R. Carruthers, G. E. Peterson, M. Grasso, and P. M. Bridenbaugh, J. Appl. Phys. **42**, 1846 (1971).

[32] H. M. O'Bryan, P. K. Gallagher, and C. D. Brandle, J. Am. Ceram. Soc. **68**, 493 (1985).

[33] T. Yamada, N. Niizeki, and H. Toyoda, Jpn. J. Appl. Phys. **7**, 298B (1968).

[34] V. Gopalan and M. C. Gupta, Appl. Phys. Lett. **68**, 888 (1996).

[35] K. Kitamura, J. K. Yamamoto, N. Iyi, S. Kirnura, and T. Hayashi, J. Cryst. Growth **116**, 327 (1992).

[36] Y. Furukawa, K. Kitamura, E. Suzuki, and K. Niwa, J. Cryst. Growth **197**, 889 (1999).

[37] L. Tian, V. Gopalan, and L. Galambos, Appl. Phys. Lett. **85**, 4445 (2004).

[38] K. Kitamura, Y. Furukawa, K. Niwa, V. Gopalan, and T. E. Mitchell, Appl. Phys. Lett. **73**, 3073 (1998).

[39] I. Bhaumik, S. Ganesamoorthy, R. Bhatt, A. K. Karnal, V. K. Wadhawan, P. K. Gupta, K. Kitamura, S. Takekawa, and M. Nakamura, J. Appl. Phys. **103**, 014108, 014108 (2008).

[40] S. H. Wemple, M. DiDomenico, and I. Camlibel, Appl. Phys. Lett. **12**, 209

(1968).

[41] V. G. Gavrilyachenko, R. I. Spinko, M. A. Martynenko, and E. G. Fesenko, Sov. Phys. Solid State **12**, 1203 (1970).

[42] J. D. Brownridge, Nature **358**, 287 (1992).

[43] B. Naranjo, J. K. Gimzewski, and S. Putterman, Nature **434**, 1115 (2005).

[44] S. C. Abrahams, H. J. Levinstein, and J. M. Reddy, J. Phys. Chem. Solids **27**, 1019 (1966).

[45] S. C. Abrahams, E. Buehler, W. C. Hamilton, and S. J. Laplaca, J. Phys. Chem. Solids **34**, 521 (1973).

[46] M. E. Lines, Phys. Rev. **177**, 819 (1969).

[47] W. D. Johnston and I. P. Kaminow, Phys. Rev. **168**, 1045 (1968).

[48] J. L. Servoin and F. Gervais, Solid State Commun. **31**, 387 (1979).

[49] A. Jayaraman and A. A. Ballman, J. Appl. Phys. **60**, 1208 (1986).

[50] C. Raptis, Phys. Rev. B **38**, 10007 (1988).

[51] Y. Tezuka, S. Shin, and M. Ishigame, Phys. Rev. B **49**, 9312 (1994).

[52] A. F. Penna, A. Chaves, and S. P. S. Porto, Solid State Commun. **19**, 491 (1976).

[53] A. Hushur, S. Gvasaliya, B. Roessli, S. Lushnikov, and S. Kojima, Phys. Rev. B **76**, 064104, 064104 (2007).

[54] G. L. Catchen and D. M. Spaar, Phys. Rev. B **44**, 12137 (1991).

[55] I. Inbar and R. E. Cohen, Phys. Rev. B **53**, 1193 (1996).

[56] K. Toyoura, M. Ohta, A. Nakamura, and K. Matsunaga, J. Appl. Phys. **118**, 064103 (2015).

[57] A. M. Glass, Phys. Rev. **172**, 564 (1968).

[58] R. C. Miller and A. Savage, Appl. Phys. Lett. **9**, 169 (1966).

[59] C. Arago, J. A. Gonzalo, and J. Przeslawski, Ferroelectrics **304**, 955 (2004).

[60] I. Tomeno and S. Matsumura, J. Phys. Soc. Jpn. **56**, 163 (1987).

[61] H. Boysen and F. Altorfer, Acta Crystallogr., Sec. B **50**, 405 (1994).

[62] H. Iwasaki, H. Toyoda, and H. Kubota, Jpn. J. Appl. Phys. **6**, 1338 (1967).

[63] R. Hsu, E. N. Maslen, D. du Boulay, and N. Ishizawa, Acta Crystallogr., Sec. B **53**, 420 (1997).

[64] Synchrotron radiation, (Wikipedia) https://en.wikipedia.org/wiki/Synchrotron_radiation.

[65] P. Willmott, *An Introduction to Synchrotron Radiation* (Wiley, West Sussex, 2011).

[66] S. Mobilio, F. Boscherini, and C. Meneghini, *Synchrotron Radiation: Basics, Methods and Applications* (Springer, Berlin, 2015).

[67] N. Ishizawa, J. Cryst. Soc. Jpn **42**, 155 (2000) [in Japanese].

[68] E. Nishibori, M. Takata, K. Kato, M. Sakata, Y. Kubota, S. Aoyagi, Y. Kuroiwa, M. Yamakata, and N. Ikeda, Nucl. Instr. Meth. Phys. Res. A **467-468**, 1045 (2001).

[69] S. Kawaguchi, M. Takemoto, K. Osaka, E. Nishibori, C. Moriyoshi, Y. Kubota, Y. Kuroiwa, and K. Sugimoto, Rev. Sci. Instrum. **88**, 085111 (2017).

[70] M. Takata, E. Nishibori, and M. Sakata, Zeitschrift für Kristallographie - Crystalline Materials **216**, 71 (2001).

[71] M. Takata, E. Nishibori, and M. Sakata, Materia Japan **40**, 267 (2001) [in Japanese].

[72] H. Rietveld, J. Appl. Crystallogr. **2**, 65 (1969).

[73] M. Sakata and M. Sato, Acta Crystallogr., Sec. A **46**, 263 (1990).

[74] H. Tanaka, M. Takata, E. Nishibori, K. Kato, T. Iishi, and M. Sakata, J. Appl. Crystallogr. **35**, 282 (2002).

[75] K. Momma and F. Izumi, J. Appl. Crystallogr. **44**, 1272 (2011).

[76] A. J. C. Wilson, *INTERNATIONAL TABLES FOR CRYSTALLOGRAPHY* (Kluwer academic publishers, Dordrecht/Boston/London, 1995), Vol. C.

[77] C. Kittel, *Introduction to Solid State Physics* (Wiley, New York, 1996), 7th edn.

[78] M. Sakata, M. Takata, and E. Nishibori, Solid State Phys. **35**, 707 (2000) [in Japanese].

[79] M. Takata and M. Sakata, Denshi kenbikyo **38**, 104 (2003) [in Japanese].

[80] T. Saka and N. Kato, Acta Crystallogr., Sec. A **42**, 469 (1986).

[81] S. van Smaalen, L. Palatinus, and M. Schneider, Acta Crystallogr., Sec. A **59**, 459 (2003).

[82] R. R. Choudhury, R. Chitra, F. Capet, and P. Roussel, Journal of Molecular Structure **994**, 44 (2011).

[83] D. V. R. Y., B. W. J., and F. D., Acta Crystallogr., Sec. A **50**, 383 (1994).

[84] Y. T, Master thesis, Hiroshima University, 2013 [in Japanese].

[85] M. Takata, Acta Crystallogr., Sec. A **64**, 232 (2008).

[86] I. D. Brown, Chem. Rev. **109**, 6858 (2009).

[87] I. D. Brown and D. Altermatt, Acta Crystallogr., Sec. B **41**, 244 (1985).

[88] S. Adams, Solid State Ionics **136-137**, 1351 (2000).

[89] H. Iwasaki, N. Uchida, and T. Yamada, Jpn. J. Appl. Phys. **6**, 1336 (1967).

[90] H. Tanaka, Y. Kuroiwa, and M. Takata, Phys. Rev. B **74**, 172105 (2006).

[91] J. Harada, T. Pedersen, and Z. Barnea, Acta Crystallogr., Sec. A **26**, 336 (1970).